MONITORING AND MODELING LONG-TERM ENVIRONMENTAL INFLUENCES ON A SHALLOW EXCAVATION USING MACHINE LEARNING: CASE STUDY OF TOMB TT95 IN THE THEBAN NECROPOLIS, LUXOR, EGYPT.

Apostolos Vasileiou

A Thesis submitted to the Faculty of Graduate Studies in Partial Fulfillment of the Requirements for the Degree of

Master of Applied Science

Graduate Program in Civil Engineering

York University

Toronto, Ontario, Canada

August 2024

ABSTRACT

Exposure of rock in thermal cycling has been linked to reduction in intact rock sample strength at a laboratory scale and has been characterized as a potential triggering mechanism for rock falls. However, the long-term effect of climatic fluctuations on shallow rock excavations still remains unknown. This research investigates the long-term effects of climatic fluctuations on shallow rock excavations by monitoring a damaged pillar in TT95, an underground funerary chapel in Theban Necropolis, Luxor, Egypt. Using two orthogonally placed extensometers, relative displacements of the pillar were measured alongside temperature and humidity. Findings indicate that pillar displacements correlate with seasonal temperature changes, showing a 0.02 mm/year drift. Data-driven CNN models were developed for forecasting, with one extensometer model achieving high accuracy (R^2: 0.98) and the other performing poorly (R^2: -0.2). The study suggests that continued pillar drift could cause loose rock blocks on the chapel ceiling to detach over time.

PREFACE

Personal Contributions to this Research

This thesis represents the culmination of my contributions to the geological investigations conducted as part of the Swiss Egyptological Mission at Sheikh Abd El-Qurna hill, under the broader Life Histories of Theban Tombs project led by the University of Basel. Specifically, my work builds upon the foundational efforts initiated by the geological research group of the project in April 2018 under the guidance of Professors Martin Ziegler (ETH) and Matthew Perras (York University). When I joined the project in September 2021, I became part of an ongoing investigation into the structural integrity and environmental conditions within Tomb TT95.

At the time of my involvement, the monitoring system within TT95 consisted of two extensometers monitoring pillar K and two Inkbird weather sensors, each with limited data storage capacity and no remote data retrieval mechanism in place . This constraint necessitated frequent site visits to manually retrieve data, posing challenges for continuous and comprehensive monitoring.

My primary contributions to the monitoring project came during two field missions in February and August of 2022. During these missions, I designed and implemented significant upgrades to the existing monitoring system. I developed a custom Raspberry Pi-based logging module that centralized and expanded data storage, allowing all monitoring instruments to feed data directly into this system. This improvement not only extended the system's data retention capacity but also enabled remote data transmission to the project’s database, eliminating the need for on-site data retrieval. Additionally, I integrated Arduino-based climate sensors into the system, further enhancing its monitoring capabilities. Beyond these technical contributions, I utilized the retrieved monitoring data for exploratory data analysis and machine learning research. These analytical efforts, forming a major part of this thesis, were my independent contributions, showcasing the potential for data-driven insights into the structural and environmental conditions of TT95.Contributions to the scientific community

As a result of this research, I presented my findings at the 22nd Rock Mechanics Symposium (RockEng) organized by the Canadian Rock Mechanics Association in August 2022 in Kingston, Ontario. My poster, titled “Numerical and Machine Learning Based Approaches to Study the Influence of Environmental Conditions on Crack Growth in the Theban Necropolis, Egypt” [1], was well-received and is included in the appendix of this document. The presentation also led to the publication of my work in the conference proceedings, marking a meaningful contribution to the scientific community by highlighting how interdisciplinary approaches can address challenges in the preservation of cultural heritage.

ACKNOWLEDGEMENTS

This thesis would not have been complete without the tremendous support and contributions of many people, whom I want to thank personally.

I extend a special shoutout to my family—my father George, my mother Soultana, my brother Thomas, and my life partner Vasiliki—for their incredible support and motivation throughout the work needed to complete this research.

I also want to thank all my dear friends, especially Pavlo, Andrea, Dimitri, Dimitri, and Christo, for always cheering me up and supporting me when things didn't go as planned during this research and other hardships I encountered.

Words cannot express my gratitude to my incredible supervisors, Dr. Matthew Perras and Dr. Usman Khan, for their guidance, mentorship, inspiration, and patience. They provided the foundation for the fruitful career I aspire to have.

Special acknowledgments go to Dr. Susan Bickel, director of the University of Basel Kings' Valley Project, and Dr. Andrea Loprieno-Gnirs from the Department of Ancient Civilizations at the University of Basel, for their mentorship and Egyptological expertise.

I also thank:

Andrew Hyett and YieldPoint for subsidizing the high-precision extensometers and data loggers used in this work.

Dr. Martin Ziegler along with the geodesy research group supervised by Prof. Andreas Wieser from ETH, whose past research in the Valley of the Kings and SAQ provided essential background and access to photogrammetry data and 3D models of TT95 and the SAQ hill.

Rodrigo Alcaino-Olivares offered guidance, support, and knowledge sharing from his PhD research in KV42 in the Valley of the Kings.

Lastly, I am grateful to the Ministry of Tourism and Antiquities and its branch in Luxor and the West bank, along all the Egyptian colleagues who assisted with fieldwork during site visits; their contributions were invaluable.

CONTENTS

TABLE OF FIGURES

LIST OF TABLES

1 INTRODUCTION

The Theban Necropolis, located near Luxor, Egypt, proudly boasts the prestigious United Nations Educational, Scientific and Cultural Organization (UNESCO) World Heritage designation. Within its grounds are hundreds of rock-excavated funerary chambers and halls, once the final resting places of ancient Egyptian elites. Situated on the West Bank of the Nile River, opposite the city of Luxor, the Necropolis extends along the ridge of the Theban Plateau, consisting of limestone strata which rises above the western side of the Nile floodplain. The deep wadis and foothills of the Theban Plateau, carved into the limestone from heavy rainfall over the passage of time, host the historic burial sites, chambers and other structures of significant cultural and religious significance the Necropolis comprises [2].

Thebes emerged as a powerful cult center for the god Amen-Ra, the principal deity of the Egyptian state during the New Kingdom period, spanning from 1570 B.C. to 1070 B.C. [3]. The religious significance of Thebes is evident through the presence of impressive temples and burial sites for the Pharaohs, the rulers of the Egyptian state during the 18th-20th dynasties (the dynasties of the New Kingdom) and other members of the ancient Egyptian elite. Among these burial sites, belong the Valley of the Kings, which hosts dozens of royal tombs excavated into the cliffsides of the Theban Limestone and the hill of Sheikh Abd El-Qurna (SAQ) which accommodates hundreds of rock-excavated tombs that belonged to the elites and nobles of the state, such as high priests, and viziers [4].

This research focuses on the case of TT95, a tomb situated on the SAQ hill, which belonged to the ancient Egyptian Mery, who served as a high priest of Amen during the 18th Dynasty (1550-1292 BC). TT95 was built during the reign of king Amenhotep II, apparently during the last three decades of the 15th century BC and is a subsurface pillared tomb that has withstood the passage of millennia showing levels of structural degradation. A prominent, large open fracture traverses the tomb, nearly splitting it in two, and has played a pivotal role in its partial collapse. This fracture extends through one of the tomb's pillars, and, in combination with the detachment of a wedge-shaped block near its top, has left the pillar in a damaged state.

The age and location of TT95 gives the unique opportunity to observe and study long-term influences of climatic conditions on the host rock of this shallow excavation. TT95 was built more than three thousand years ago, meaning that it has been subjected to thousands of thermal cycles over its lifetime. The warm and arid climate, with large intraday temperature variations and virtually no precipitation, gives the opportunity to isolate and study the effect of heat cycles on the rock mass quality.

1.1 Thermal Cycling As A Degradation Mechanism of Rock

The literature review below summarizes a few studies that researched the influence of daily and seasonal fluctuations on rock behaviour. Research has mostly focused on laboratory studies, rock slopes and cliffs, as well as deep geological repositories that will host radioactive waste that drives a thermal pulse through the rock mass.

1.1.1 Effect of Heat Cycles in Lab Specimens of Intact Rock

Studying thermal influence on laboratory specimens is a common method used in many fields to examine the thermal behaviour of rock. This includes geological studies related to Earth dynamics (REF) to those focused on radioactive waste and intact rock properties at elevated temperatures. The later is closer to the temperatures that rocks are subjected to the Earth's surface [5] with the former being beyond the scope of this thesis. Gautam et al. (2021), examined the characteristics of granitic rock lab specimens to investigate the suitability of the Jalore Granite as a host rock for a nuclear waste geological repository [6]. In their study the researchers imposed 9 cycles of heating and cooling to the granitic specimens, by heating the specimens to 250^0C at a constant heating rate, where they were kept for 12 hours and then cooling them down at a constant cooling rate, for a total of nine cycles. What they discovered was that the thermal cycling caused an accumulation of strains within the samples, and a reduction in rock strength. The weakening of the rock was becoming more pronounced progressively with each cycle until the fifth cycle, past which the damage on the specimens was not increasing any further.

Feng et al. (2020) also conducted lab testing of granitic specimens, exposing the samples to a temperature range of 20-300^{o}C for 1-20 cycles [7], in an experiment for evaluating feasibility of constructing geothermal systems. They also found that the fracture toughness of the granite samples is reduced considerably in the first five cycles, while plateauing past that point. They attributed their findings to the thermal cycling promoting initiation and propagation of intergranular and intragranular cracks, which increased the crack density within the rock samples, decreasing their resistance to fracture.

These cyclic tests, although at higher temperatures than the Earth's surface in a desert environment, reflect the cyclic nature of the thermal fluctuations the open rock surfaces are exposed to.

1.1.2 Effect of Temperature Fluctuations on Open Rock Surfaces

Research motivated by rockfalls, and rockslides initiated in the absence of known and well documented triggers, such as precipitation, earthquakes and freeze-thaw cycles, has suggested that the small diurnal and seasonal temperature perturbations rock is exposed to, can enhance the efficacy of other known rock-fall triggers or even initiate one on their own by promoting fracture opening and propagation over time [8], [9], [10].

Gunzburger et al. (2005) studied the influence of daily surface temperature fluctuations in the stability of the Rochers de Valabres slope, in France [8]. The slope failed in May 2000, causing substantial economic and social interruptions. The slope failed without the precedence of a known trigger (precipitation, earthquake, freeze-thaw period). In an attempt to investigate the unknown trigger of the rockslide, the researchers hypothesized that continuous surface temperature perturbations served as a mechanism to drive long-term crack growth for the rockslide with a cumulative effect. Their hypothesis was enhanced by constructing a numerical model showing thermally induced deformations can cause a creep effect that can potentially mobilize a rock block placed in a near unstable position. Their research also included the use of a combination of a high-precision geodetic system with a weather station on a sensitive portion of the remaining slope. The results of study concluded that while surface temperature changes act as a preparatory factor for rockfalls, their direct influence is hard to be quantified, particularly due to the limitations in measurement accuracy by their geodetic monitoring system.

Collins and Stock (2016), also interested in studying rockfalls that occurred without the existence of a known triggering mechanism, observed, and monitored an exfoliating granite cliff in Yosemite National Park, California, USA [11]. They focused on monitoring a 19 m tall, exfoliated granite sheet using crack aperture data, in conjunction with measuring light intensity, humidity, and temperature. Their results showed that the crack aperture trends correlated with the trends of the air-temperature near the rock surface. They also observed a bounded hysteretic response of the crack aperture with temperature, in which heating and cooling cycles followed parallel but different pathways through time (Figure 1). The highest outward deflections of the sheet were observed during the hottest months of the year and the authors suggested that this is the time with the highest risk of rockfalls due to the exfoliated sheets having their highest outward deflection. The study also included a thermodynamic analysis in which the authors showed that daily, seasonal and annual temperature variations are sufficient to drive cyclic and cumulative opening of fractures.

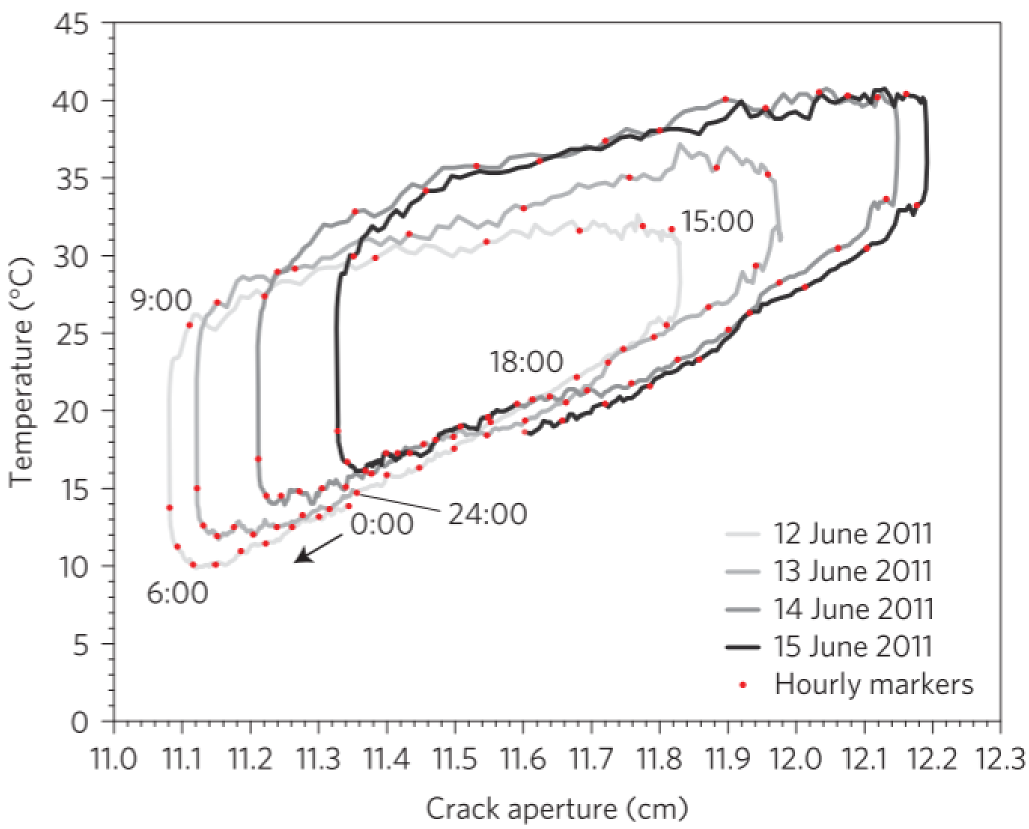

Figure 1: Temperature-Crack aperture plot showing the hysteretic cycling behaviour of the crack aperture in response to daily temperature variations (image from Collins and Stock (2016) [11]

Barbier et al. (2021) monitored a limestone cave next to the small French village of La-Roque Gaceac [9]. Their study was also a monitoring experiment in which they installed fissurometers on some of the cave fractures to log the fracture aperture over time, along with temperature measurements of ambient air and rock, at depths of 2m and 6m. The study examined 5 years of monitoring data. The authors of this study also found that temperature variations correlated with fracture aperture, and a similar hysteretic behaviour with small permanent deformations accumulating on a yearly basis was present in this study as well.

KV42 is a tomb in the adjacent site of the Valley of the Kings, the burial place for most of the kings during the New Kingdom. Outside the entrance of KV42, there is a rock column that is overhanging just above the entrance to the tomb. The column is attached through its base to the limestone cliff of the Theban Limestone Plateau, which surrounds the Valley of the Kings. Above its base, the column is separated by the cliff and an open fracture lies between them. Similarly to the works of the previous subsection, the aperture of the fracture was monitored via a crack meter and analyzed with collected trends of temperature and humidity measurements with a weather station on the cliff face. Cyclic deformations have been linked to both temperature and humidity variations throughout the year. Thermal-mechanical numerical modelling has been used to decern the thermal component of the cyclic deformations. Although thermal heating and cooling is a key driver, it is not the only force driving deformation and multi-year monitoring indicates permanent increased deformation of a critical crack that could lead to collapse of the cliff at some point in the future. However, according to Alcaino-Olivares et al. (2022), the cliff has been in its current state since the tomb KV42 was unearthed over 100 years ago. This speaks to the complex nature of thermal fatigue, that can lead to degradation of the rock over extended periods of time.

1.2 Rehabilitation of Royal tombs in the Valley of the Kings

Deterioration and structural degradation have also been observed in some of the royal tombs found in the Valley of the Kings [12], [13] [14]. Generally, the royal tombs were constructed with much higher-quality rock, unlike the tombs in the SAQ hill. The royal tombs in the Kings Valley were typically excavated in rock of superior quality. However, an exception arises for those situated near the boundary between the Theban Limestone and Esna shale, where swelling appears to be the primary source of damage [14] Although many of the royal tombs have deteriorated, the mechanisms differ due to variations in location, rock mass formation, and the geomorphology of the local environment at the two sites.

Research investigating the damage to royal tombs in the Valley confirms that flash flooding has significantly contributed to structural issues, as observed in KV5 [15]. Despite the close proximity to the Valley, the landscape surrounding TT95 and its neighboring tombs differs significantly. The massive cliffs surrounding the valley can channel a substantial amount of runoff water into the valley during a "flash-flood" event, potentially flooding a tomb entirely. In contrast, although the same event could still cause considerable damage to the tombs in SAQ due to debris flow and erosion, the steep slopes around the tombs divert water away from the tombs toward the alluvial plain of the Nile. Consequently, the physical processes driving structural degradation can vary entirely between tombs in SAQ and those in the KV, even though both may originate from the same natural event.

Geological differences between the royal tombs and those in SAQ are also crucial for assessing the damage in TT95 and making meaningful comparisons with those in the VOK. Most of the Valley's tombs are excavated within Member 1 [1] of the Theban Limestone Formation, with some extending deeper into the Esna shale. However, the tilted block comprising the SAQ hill led to the excavation of those tombs within Members 3, 4, and 5[1], situated at a considerably higher elevation near the valley. Subtle variations in the rock material, such as those between different members of the formation, must be considered when assessing the damage in TT95 and selecting an appropriate rehabilitation method, as strength and fracturing characteristics may differ.

Additionally, the excavation depth varies significantly between the tombs in the valley and those in SAQ. TT95 is a near-surface excavation with overburden not exceeding a few meters at most. In contrast, the royal tombs are mostly excavated at the base of the

[1]. For an in-depth explanation of the Theban Limestone Formation Unit Members see Chapter 2.

Theban hills, subject to much greater geostatic stresses as overburden depths exceed one hundred meters [16]. Consequently, fracture behavior differs significantly in the two cases, as fractured rock near the surface is much looser and easier to mobilize than fractured rock at greater depths, which is constrained by the clamping forces caused by the geostatic stress surrounding the tomb excavation boundaries.

1.3 Problem Statement, Research Gap, and Study Objectives

As of the author's knowledge, there is currently little to no published research that investigates the influence of environmentally induced thermal cycles on the stability of near-surface rock excavations. The literature review conducted showed that similar monitoring projects have only been conducted on exposed rock surfaces and cliffsides, and that the theoretical framework for explaining the weakening of intact rock under thermal cycling, has only been established through lab testing of rock samples obtained for projects that are related to deep underground projects and are exposed to short and more intense heating cycles (temperature wise) than those of natural ambient temperature cycles alone.

TT95 is a shallow excavation in limestone rock, where the rock mass regime is different than that of a cliffside. The underground structure of TT95 extends the work that was conducted on cliff and rock exfoliated sheets since the structure and void space of the excavated rock in TT95 alter the mechanics and stress fields within the rock mass. On top of that, the age and location of TT95 presents a unique opportunity to explore the long-term effects of environmental fluctuations, including temperature and humidity, on the degradation of the host rock mass and its overall stability. Contrary to the lab experiments reviewed above, the range of the heat within a given cycle is much smaller as ambient conditions do not reach the ranges of an underground nuclear repository or geothermal reservoir, and the exposure to thermal cycles has been undergone for millennia and is not limited to a few tens of cycles. This study aims to address the knowledge gap of environmental fluctuation influence on shallow limestone excavations.

Additionally, TT95 is experiencing considerable structural degradation. This study aims to examine what is the influence, if any, of climatic fluctuations on the stability and rock quality of TT95 and its host rock, so that this influence can be accounted for in future projections of the stability of the tomb. To address these research questions, the following research objectives have been developed:

- Collect data on the long-term behaviour of rock mass in a shallow excavation exposed to environmental fluctuations for millennia
- Examine and study the response, if any, of the rock mass temperature and humidity trends as captured by relative displacements between pillars measured by extensometers
- Use a data-driven modelling approach by applying Machine Learning (ML) algorithms to obtain insights on how temperature and humidity variations affect the behaviour of the rock mass in TT95
- Establish a knowledge basis to serve as a guide for future rehabilitation of TT95 and other tombs in the area subject to similar degradation

1.4 Thesis Outline

This thesis is organized into a total of six chapters.

Chapter 2 of this thesis summarizes important background knowledge about tomb and the wide area of the site, as well as some literature review of what inspired the methodology taken in this research. A background search and review of other research applications of ML in Civil Engineering is also presented in this chapter, to bring the reader up to speed with the approaches and methodology presented in subsequent chapters.

Chapter 3 presents the methodology that was used in this research. The monitoring setup is explained in detail along with the exact steps that were taken to process and analyze the data collected. The raw collected data are introduced to give the reader a sense of what type of data have been collected, which has strongly influenced the approach taken to analyze them. The methodology chapter also outlines how ML was utilized on the collected datasets to help extract meaningful insights from the collected dataset.

Chapter 4 outlines the results of the methodology outlined in Chapter 3, applied on the collected dataset from the monitoring system.

Chapter 5 discusses the results that are presented in the previous chapter and analyzes how those results fit into understanding the observed behaviour of the rock in TT95, within the context of the research project.

The final chapter, Chapter 6, provides conclusions and important connections between the research objectives and the findings.

2 BACKGROUND

2.1 SITE LOCATION

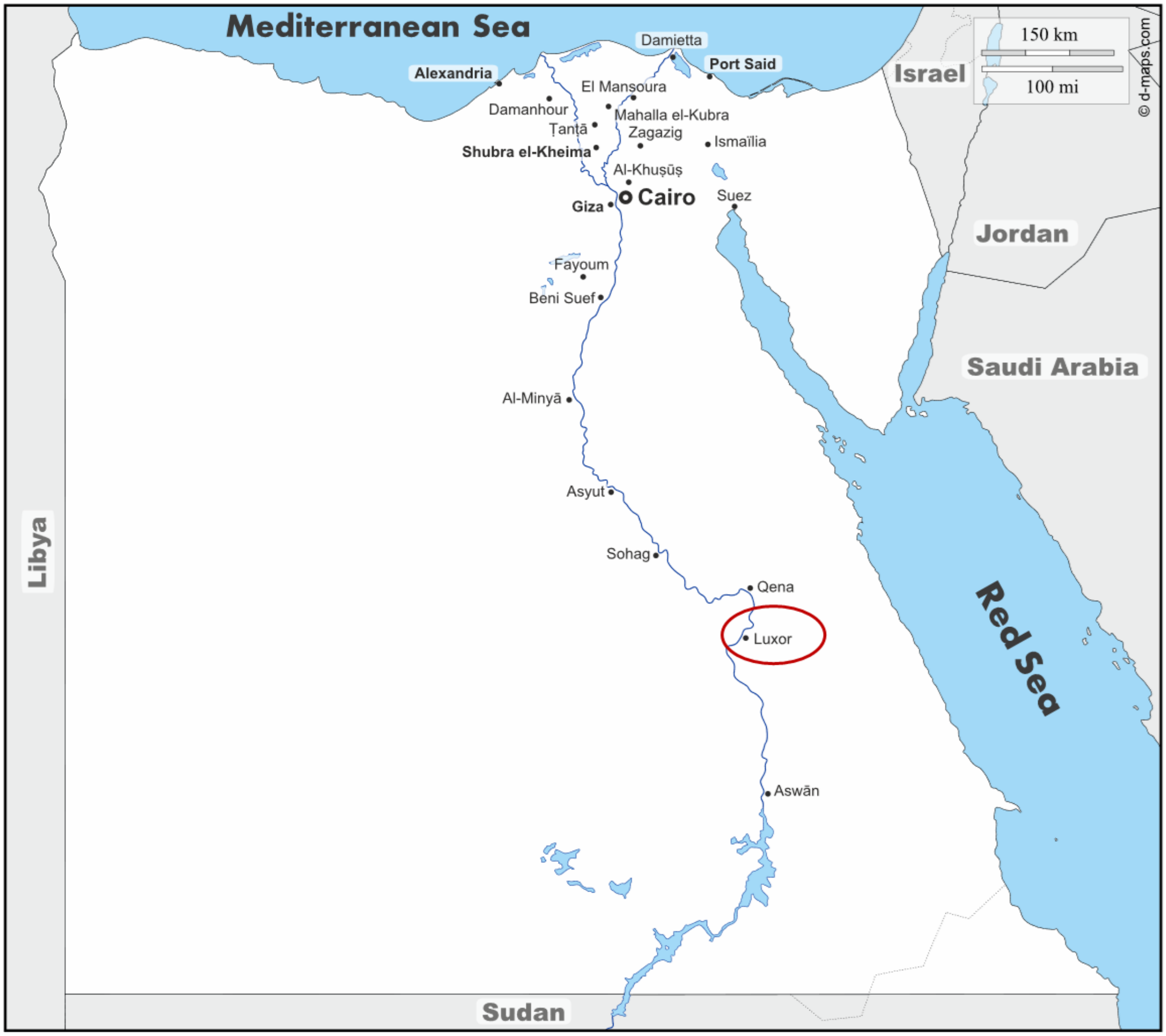

Figure 2: Map of Egypt, showing the study location, Luxor, circled in red within the regional context.

The ancient city of Thebes and its Necropolis are located on the banks of the Nile River, where currently sits the modern city of Luxor, which lies about 500 km South-Southeast of Cairo, Egypt's capital city (Figure 2). On the east bank of the river, Luxor hosts impressive monuments, like the ancient temples of Karnak and Luxor, amongst others. On the Nile's West Bank, the Necropolises of the Valley of the Kings, and Valley of the

Queen’s which served as burial places for the “Pharaohs”, the ancient Egypt kingdoms’ rulers, have stood the passage of time and have become a popular worldwide attraction.

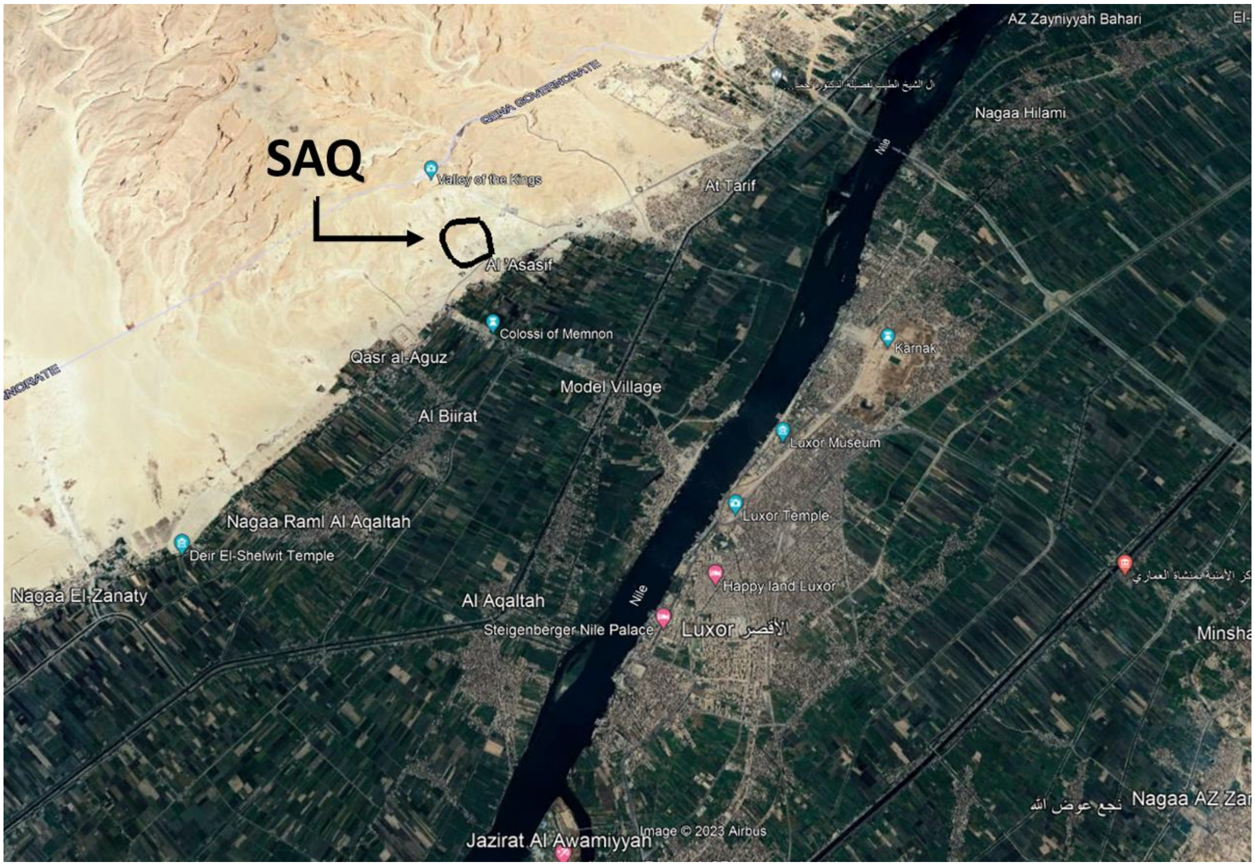

Figure 3: Location of the SAQ hill, across from the City of Luxor, Egypt, where the shallow tomb TT95 has been constructed near the edge of the Nile River flood plain and the Theban plateau [17].

The SAQ hill is located on the West Bank of the Nile, adjacent to the Valley of the Kings Figure 3. The entire hillside of SAQ is draped with little voids, that are the entrances to the tombs built on the hill, which gives a characteristic look that separates it from the Theban Plateau cliffs on the background (Figure 4).

Figure 4: View of the SAQ hill in front of the cliffs of the Theban Mountains. TT95 is located just above the base of the hill, as indicated in the figure.

2.2 TT95

2.2.1 TT95 Geometry

TT95 is a rock-cut subsurface pillared tomb excavated on the hillside of the SAQ hill. The tomb consists of two chambers. The main (East) chamber is a rectangular transverse hall (17.5 m x 8.3 m) with high ceilings, supported by 12 pillars, oriented along the North-South direction, with its entrance facing East. The secondary (West) chamber has an unfinished rough shape and is supported by 4 pillars.

The North part of the main chamber has a finished appearance and is fully decorated with the exception of the North wall. The south part of the chamber was found in a semi-finished condition, with its East wall being fully decorated. Moving towards the West wall of the tomb's south part, the conduits and pillars are not decorated and have a rougher, unfinished-like appearance (Figure 7).

Figure 5: Entrance and facade of TT95. The image highlights the direct exposure of the rock to the climate at the ground surface. The infilled open fracture can be seen to the left of the entrance.

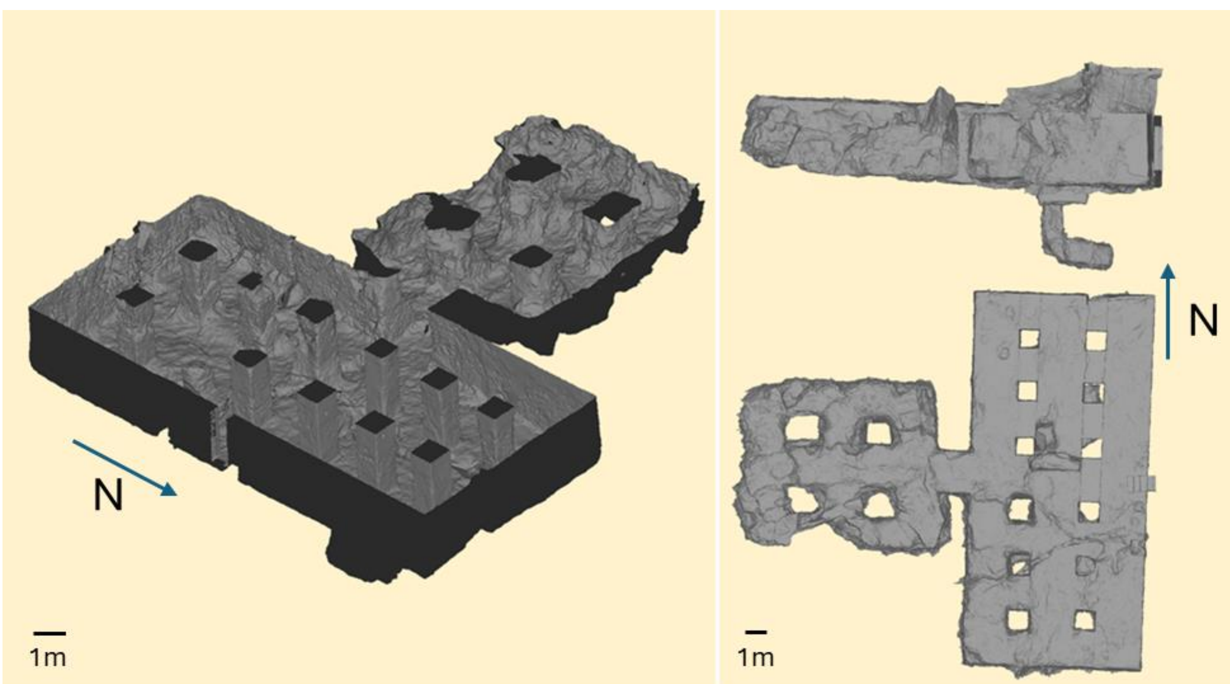

Figure 6: Perspective view (left), profile cross section (upper right) and top view (bottom right) of the 3D reconstructed model of TT95 (provided by the University of Basel's Life Histories of Theban Tombs [4])

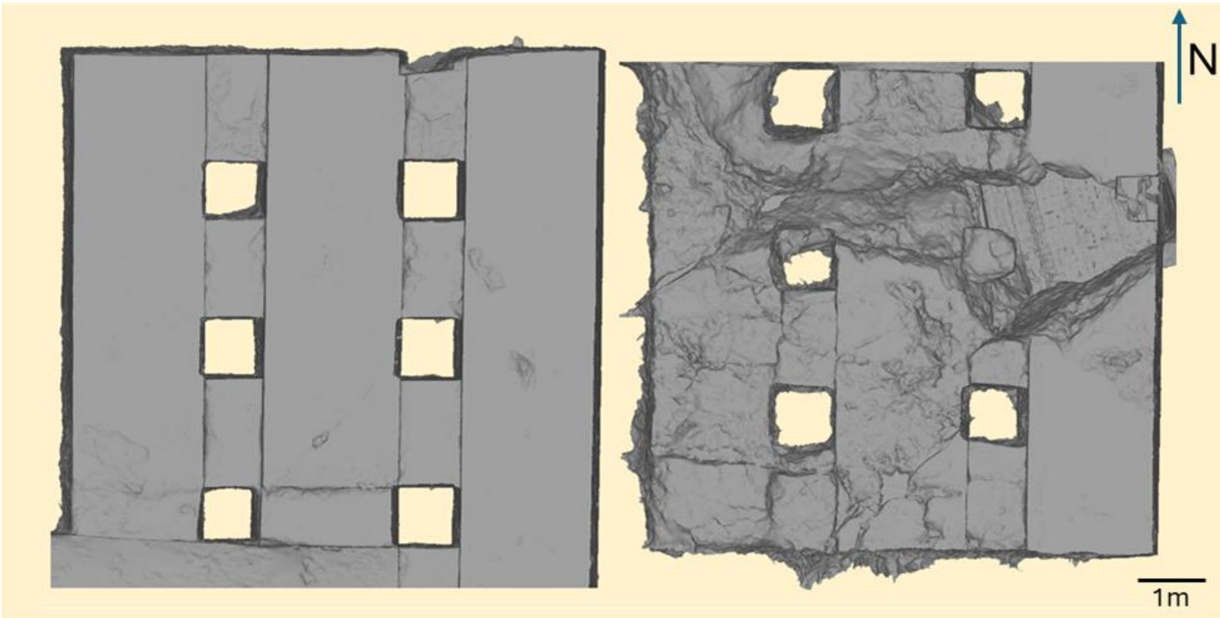

Figure 7: Comparison of the ceiling surface texture between the north (left) and south (right) parts of the main chamber (provided by the University of Basel's Life Histories of Theban Tombs[4]*).*

2.2.2 Site Geology

Three geological formations are prevalent in the area surrounding the SAQ hill which are responsible for its formation, the Theban Limestone Formation, the Esna Shale Formation and the Tarawan Chalk formation. The Theban Limestone Formation dominates the landscape of the Theban Plateau and the cliffs surrounding the SAQ hill. It is the top-most layer and overlays the Esna Shale Formation, with the chalk layer being the deepest.

The Thebes formation has been investigated by research focusing on its stratigraphy, however little agreement exists on the number of units dividing the full depth of the formation, ranging from 4 to 13 [18] [19], [20], [21]. This work adopts the stratigraphic units from Dupuis et al [18], also used as a basis by Ziegler for their geological investigation of SAQ [19]. The members of the formation are differentiated by the texture of the limestone, the marl and chert content and other geological differences.

The SAQ was formed by rotational slumping of the cliffside of the Theban Plateau [18]. The thin shale layer between the limestone and the Tarawan Chalk, sheared off by the overburden weight, and the entire cliffside slid, causing the entire block to tilt into what now is the SAQ hill.

TT95 resides within Unit 2 and Unit 3 members, which share many similarities and are both predominantly composed of massive limestone.

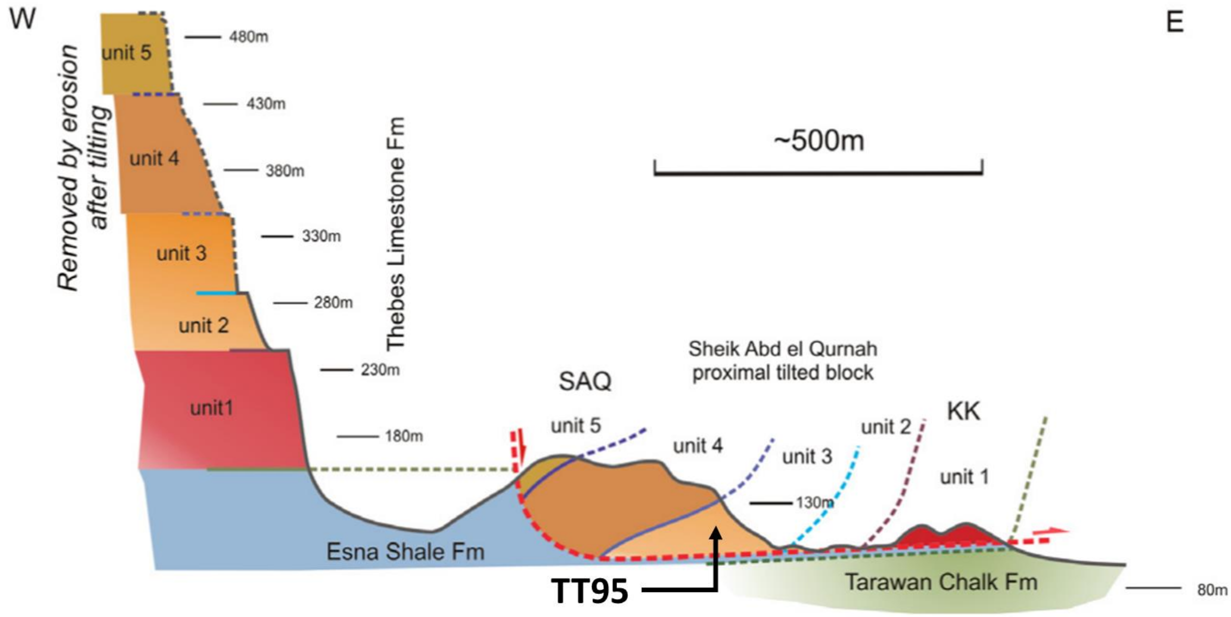

Figure 8: Geological origin of SAQ hill, and lithostratigraphy of the hill and the adjacent cliffs of the Theban Limestone Formation (modified from Dupuis et al. (2011) [18]*)*

2.2.3 Geomechanical conditions in TT95

A large open fracture cuts through the main chamber of the tomb (Figure 9) and is believed to be responsible for the partial collapse of TT95 by serving as a release plane for a large wedge-shaped block that detached from the ceiling. Underneath the void space previously occupied by that block are the remains of a fully collapsed pillar (Pillar H, Figure 9) which was previously supporting the collapsed block. The open fracture also cuts through one of the main chamber pillars (Pillar K, Figure 10) adjacent to the fully collapsed one, leaving it in a damaged condition. The main open fracture starts crossing the façade about 2m south of the tomb's entrance and cuts through the entire cross section of the first chamber. The open fracture width is approximately 20cm and has been sealed. The fracture is open and can be easily traced along the ceiling and floor of the tomb (Figure 11, Figure 11). Along the ceiling the fracture merges with the void space that is left by the detached missing wedge block right above the remains of the collapsed pillar H (see Figure 9).

Figure 9: Open fracture on the facade wall, leading to void space on the ceiling caused by the collapse of a wedge-shaped rock block.

Figure 10: Main open fracture crossing the south hall of the main chamber (left). Open fracture crossing the critical pillar K (right).

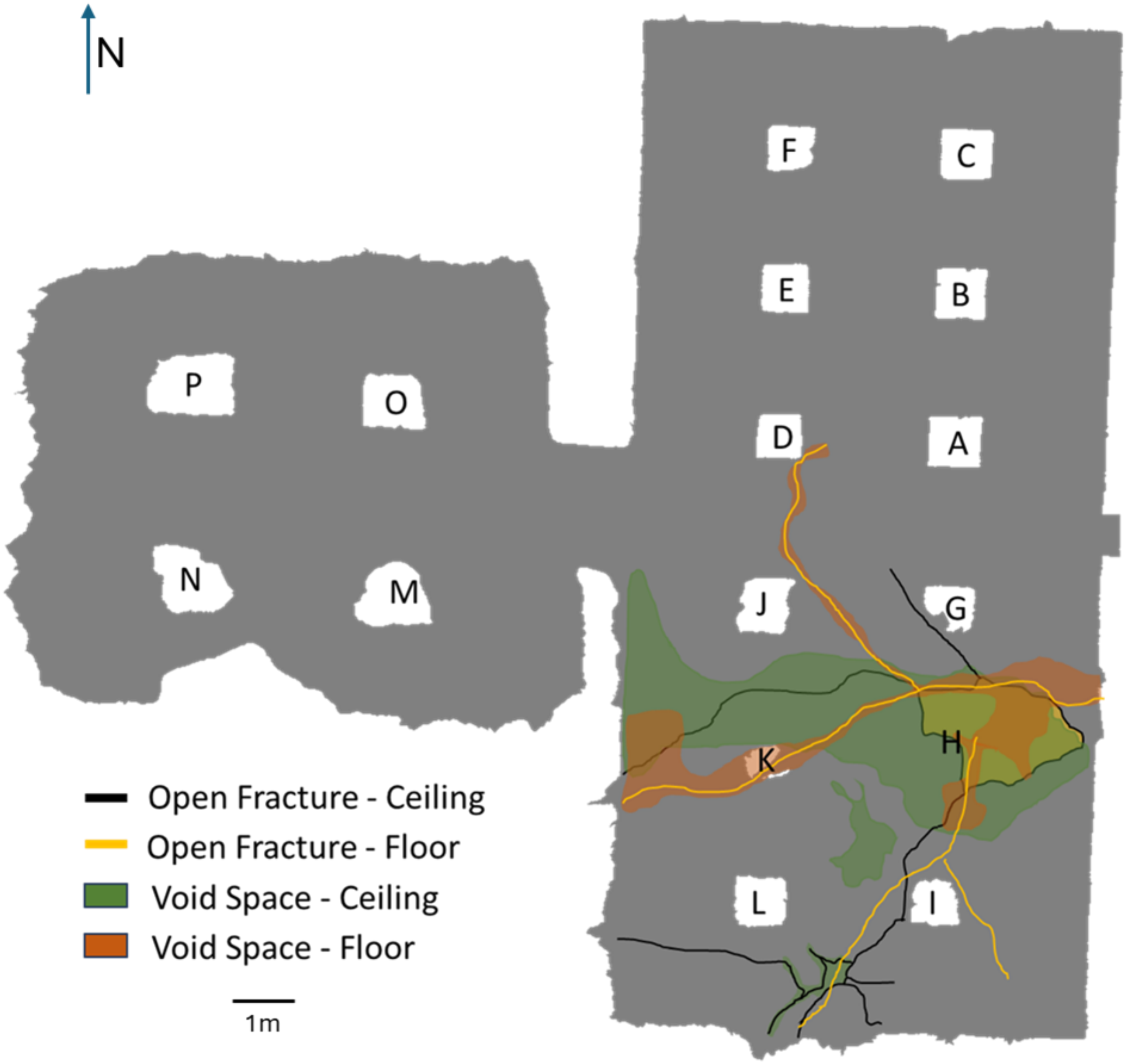

Figure 11: Fracture network along the floor and ceiling of TT95, showing both open fractures and void spaces for the ceiling and floor separately, as observed by the authors.

As discussed above, the fracture network that goes through TT95, shown above, is a result of the rotational slumping of the rock of the SAQ hill. By tracing the fractures along the ceiling of the tomb, a big block of rock supported by pillars K and L can be observed. Accordingly, the fracture trace on the floor seems to resemble, and align with, the fracture traces of the ceiling. This observation leads to the conclusion that the large block supported by the two pillars is the result of excavating through the tomb, removing material from the rock slab that was formed between its surrounding fractures, which are the result of the slumping of the hill. The isolated ceiling block is shown in Figure 12 below.

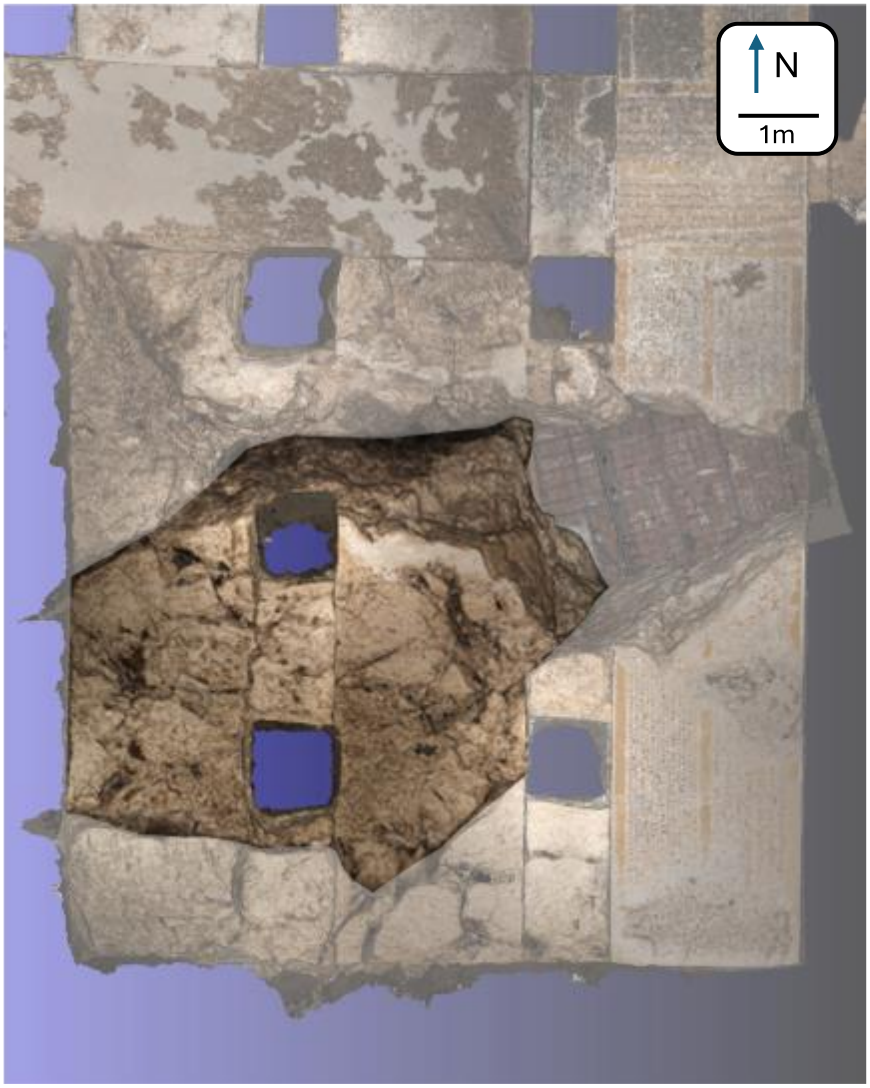

Figure 12: Isolated rock block in the ceiling surrounded by the fracture network on the south hall of the main chamber

2.3 Using ML As A Data-Driven Modeling Approach

ML (ML) has gained significant attention in various scientific fields, including civil engineering and rock mechanics. It offers powerful tools for analyzing complex data, making predictions, and aiding in decision-making processes. In this literature review, we will explore how supervised learning, artificial neural networks (ANNs), and Convolutional Neural Networks (CNNs) have been applied in the context of monitoring the stability of ancient Egyptian tombs within the Theban Limestone formation.

2.3.1 Supervised learning and Artificial Neural Networks

Supervised learning is one of the fundamental approaches in ML. In this approach, a model learns to make predictions based on labeled training data. Labeled data means that each example in the training set has a corresponding known outcome or label. Supervised learning algorithms aim to generalize patterns from this labeled data to make accurate predictions on new, unseen data. Linear regression, decision trees, and artificial neural networks are examples of supervised learning methods commonly used for regression and classification tasks [22].

Artificial Neural Networks (ANNs) are computational models inspired by the human brain's neural architecture [23]. ANNs consist of interconnected layers of processing elements, or neurons, which can capture intricate relationships within data by adjusting the synaptic connection between neurons. ANNs learn by example, through a learning process that involves seeing the labeled data, and adjusting the connection weights of its neurons to reach a state at which it can approximate the labeled data to a reasonable accuracy by only passing it its inputs. This processes is commonly known as Backpropagation [24].

2.3.2 Convolutional Neural Networks

Convolutional Neural Networks (CNNs) are a specialized type of ANN often used in conjunction with datasets consisting of images or sensor data. CNNs have been established amongst the best Deep Learning (DL) algorithms and has become the most widely used algorithm in the field of ML, with applications in cybersecurity, natural language processing, bioinformatics, and many others [20].CNNs provide two important advantages. First, CNNs have been shown to deal well with massive datasets [25]. Second, CNNs perform very well in tasks where the inputs are multidimensional arrays of values, where the spatial relationship between neighboring values is important to predict the observed outcome. For example, in image classification tasks which CNNs are known to perform very well, the spatial relationship between neighboring pixel values is of great importance to the model as group of neighboring pixels define certain features that compose the entire image and are important to interpret what the depicted object on the image is.

One-dimensional CNNs borrow this aspect of exploiting the spatial relationship between data points and apply it on 1-dimensional dataset, for example, time series, where the order of observations within the time series is important in identifying a signal. The ability of CNN to exploit the spatial relationships between neighboring input values, is now used as a proxy to exploit the temporal component of an input signal, as represented by the order of the sequence of the observations within a time series. 1-Dimensional CNNs are used in many applications that involve time-series analysis and forecasting, where the inputs are frequent sensor feeds, such as real time vibration-based structural damage detection [26][27], and peak electricity demand [28].

The sensor measurements series collected in this study through the monitoring system make it suitable for using CNNs to exploit the temporal influence of the environmental trends to the rock behaviour. This is achieved by using the temporal aspect of the time series data as the spatial component that CNNs are well known for.

3 METHODOLOGY

Modeling the response of the rock mass to changes in environmental factors is a complex problem. The fractured rock mass is a complicated material and its response to environmental stimuli can have a wide range of spatial variation. The methodology presented in this study followed a data-driven observational approach, comprising a monitoring installation and a data modeling process using ML algorithms to mimic the system's behaviour.

A monitoring system was designed and installed in TT95 to measure any changes in the system that would help develop an understanding of its behaviour. Measuring displacements and deformations in structural members of the tomb (pillars, beams, walls, etc.) and studying how those change over time, can give insight to the rock mass behaviour and stability state of the tomb. The collected measurements can also be used as a basis to calibrate numerical models for the tomb.

However, numerical models require an established model for the behaviour of the material, and knowledge of the physical processes that govern the system. Fractured rock masses are a very complex material to model, due to the anisotropy and the non-homogeneity of the intact rock material itself but also because of the presence of fractures that lead to altered and complex stress fields within the rock mass. Data-driven models do not rely on knowledge of the exact physical processes governing the observed systems, but rather attempt to exploit relationships between data, using statistical and probabilistic computational methods. The collected monitoring data makes the data-driven approach a suitable method due to the material complexities and unique geology of TT95.

Lastly, due to the remote location and designation of the tomb as an archaeological site, there are limitations to perform mechanical tests for extracting material properties. This makes a numerical approach even more challenging, as numerical models rely heavily on well-defined material parameters obtained from mechanical tests. Limitations on performing this testing reduce the reliability to those parameters and can result in low trust to the model.

For that reason, ML algorithms, and specifically CNNs, were used to model the displacements of the critical pillar in TT95, by utilizing the collected monitoring dataset without an explicit definition of a physical model.

The following subsections describe the monitoring equipment, development and utilization of CNNs models that were used for studying the tomb's response to changes in environmental variables.

3.1 MONITORING SYSTEM

Initial installation of the monitoring system begun in the spring of 2019 and included the placement of two extensometers with battery operated data loggers, and two battery operated Bluetooth enabled smart home sensors (described in more detail in subsections 3.1.1 and 3.1.2).

This system had a few limitations. The battery-operated setup was limited by the life of the batteries they used. The memory capacity of the loggers was also a second limitation as it was restricting the granularity of the data collected. The extensometers were set up to store a measurement every hour, while the weather stations were set to store measurements in half-hour intervals.

The last and most important limitation was that physical access to the loggers and weather stations was required for data retrieval, which is not cost-effective or even possible at times. A faulty sensor or any technical issue wereimpossible to identify without visiting the site, which added to the complexity of the repair and data collection processes.

To overcome these limitations, two site visits happened in February and August of 2022, in which the system underwent significant updates. The updates were targeted to resolve the above limitations. In these site visits, the battery powered extensometers were plugged to a more reliable power source obtained from the local power grid. A Raspberry Pi computer board [29]was installed as the main control board of the installation and was used as a serial reader of the instrument feeds.

Redirecting the data feed of the extensometers from the battery-operated loggers to the control board, allowed for significantly extending the memory capacity to store measurements and facilitating the data collection process. The memory increase led to better resolution of the data, by allowing for collecting measurements every 10 minutes. Custom scripts were implemented and installed on the control board that combined the data from the extensometers to a structured file, allowing for great control on how the data were stored, as well as facilitating data cleaning and preprocessing.

In those site visits, a wi-fi modem/router was also adjusted to ensure year-round access. The router selected was compatible with connecting to the internet via cellular networks by using a simple phone SIM card with data enabled capabilities, which allowed for remotely accessing the control board of the monitoring system, enabling remote data retrieval without the need to visit the site.

While the new setup gave greater control on collecting measurements from the sensors in TT95, the smart home temperature and humidity sensors installed in 2019 did not have the capability of outputting measurements via a serial communication port and remained limited to storing measurements only on the embedded memory of the station. However, accessing and downloading the Inkbird station measurements was only possible via Inkbird's proprietary mobile application Engbird, which needed to be pre-installed on a Bluetooth enabled mobile device. This meant that weather information still needed to be retrieved manually from those sensors, requiring a site visit for data retrieval, even though the remote connectivity issues were resolved for the extensometers.

To address this, a subsequent site visit in the spring of 2023 included the installation of two temperature and humidity probes to allow for remote data retrieval of climatic information. These probes were installed near the locations of the previously installed temperature and humidity sensors with the intention of remotely gathering ambient temperature measurements. The Inkbird stations were not removed, but were left in the tomb, offering a redundancy layer for the ambient air temperature and humidity layers, and a basis to assess and compare the accuracy and precision of the new probes, relative to that of the Inkbird stations. The newly installed probes were connected to an Arduino control board [30] which was responsible for reading the signals of the probes and transmitting the temperature and humidity readings to the PI logger. The Arduino board outputs the sensor readings via a serial communication port which is connected to the main control board of the system. This converted the entire monitoring system into one that could be remotely accessed without the need for visiting the site to retrieve data.

An overview map of the monitoring system is shown in Figure 13, and a diagram explaining the system connectivity is summarized in Figure 14. The loggers, main control board, Arduino control board and wi-fi modem, were installed inside a plastic box to protect them from the dust inside the tomb and were installed in an underground pit inside the tomb, covered by a wooden panel that served as a cover to the pit (Figure 15).

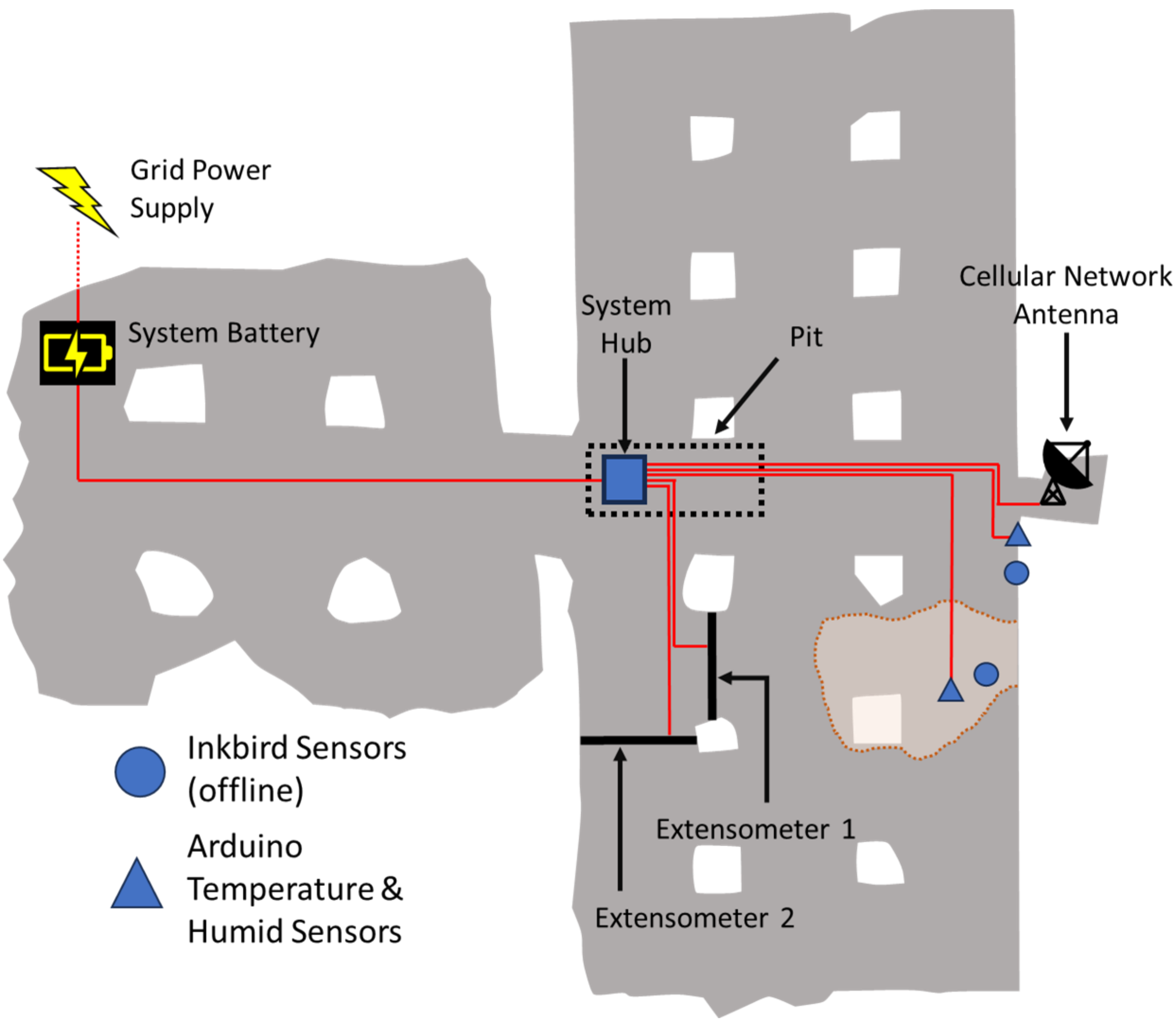

Figure 13: Map of the monitoring system setup installed in TT95.

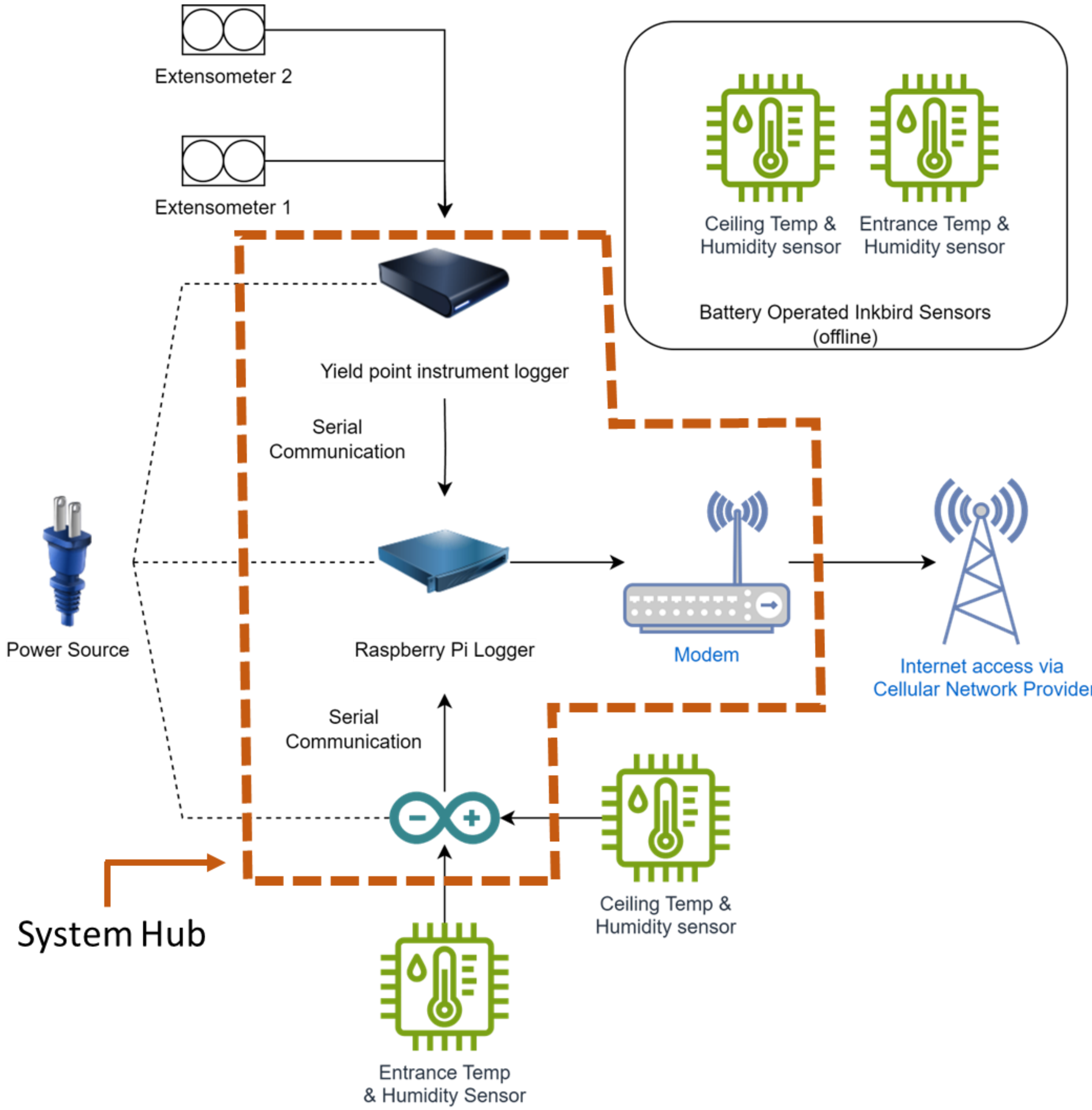

Figure 14: Monitoring system schematic diagram showing the sensor and communication connections, as well as those sensors that are offline and not integrated into the remotely accessible network.

Figure 15: Installation of monitoring system hub in the underground pit beneath the ground level of the tomb, adjacent to the vertical shaft leading to the bottom chamber of TT95

3.1.1 Pillar Displacements

The detection of displacements in the pillar of interest (Pillar K) was accomplished using two YieldPoint Extensometers arranged orthogonally. The first Extensometer (EXT1) was positioned on the North side of the critical pillar, with its other end attached to Pillar J. The second extensometer (EXT2) was placed between the west side of the pillar and the west excavation boundary of the chamber. Both extensometers cross the fracture plane projected from pillar K to the surrounding environment. The extensometers installed are high-precision instruments with a displacement accuracy of 1μm. The extensometers are also equipped with embedded temperature sensors, which were used as a proxy to monitor the interior temperature of the tomb, working in conjunction with the weather station sensors monitoring exterior air temperatures, described in detail below.

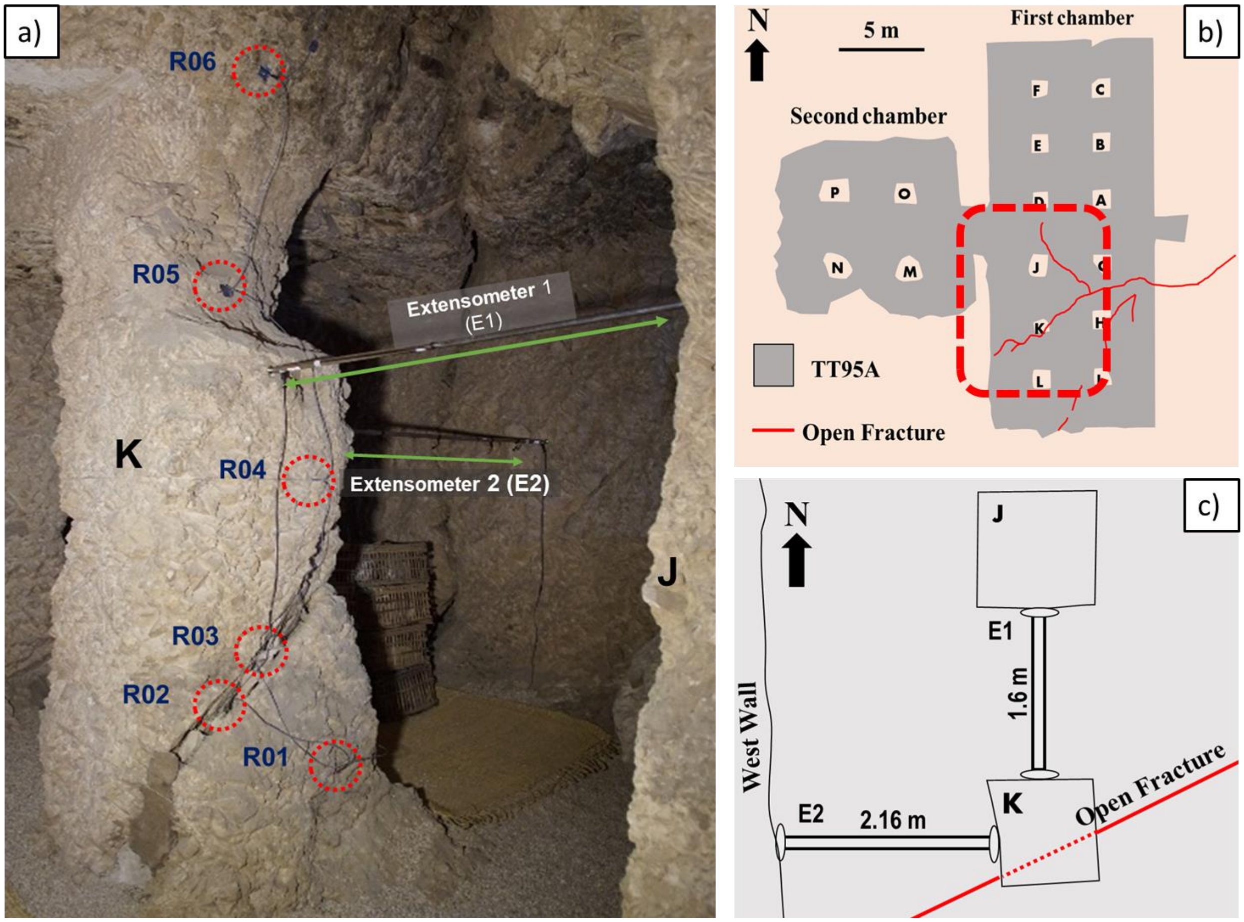

Figure 16: Extensometer layout to monitor the movement of pillar K, with a) showing the in-situ setup along with temperature sensors installed along the pillar, b) showing a plan view of the tomb and the general location being monitored, with c) specific details in plan view of the two extensometers.

3.1.2 Temperature and Humidity Monitoring

As was discussed in the literature review, temperature fluctuations can drive cyclic deformations of rocks at the laboratory scale or at the Earth's surface. In order to understand how deep thermal perturbations could penetrate the rock mass and if they or other environmental fluctuations contribute to cyclic deformations within TT95, environmental sensors have been installed. Environmental parameter monitoring was conducted using two Inkbird IBS-TH1 Thermometer/Hygrometer Bluetooth smart sensors positioned inside TT95 (Figure 16). One sensor was installed within an existing recess on the façade wall (Figure 17), with the purpose of recording ambient air temperature and relative humidity outside the tomb. The second sensor was placed within the interior of the tomb to monitor relative humidity levels inside.

The positioning of the Inkbird sensor on the façade recess meant that the sensor would not be exposed to the sun and always remained in the shade. The sun exposure duration of the façade, which is oriented to the East, was less than that of the ceiling of the tomb due to the shadow casted from the tomb in the evening hours as the sun sets. To get a better gauge of the exterior ambient temperature surrounding the tomb during the later hours of the day, the built-in thermometer of the sensor installed on the ceiling was bypassed, and a temperature probe extension cable was utilized (Figure 18). This extension cable was positioned on the metal grid covering the collapsed part of the ceiling (Figure 19). The probe was placed on a small void between the metal grid and the rock, allowing it to measure exterior air temperature near the ceiling. Consequently, while the sensor recorded interior humidity levels, it also logged the ambient air temperature outside the tomb, at a location.

Figure 17: Inkbird IBS-TH1 Bluetooth thermometer-hygrometer (image source: https://inkbird.com/products/ibs-th1-plus)

Figure 18: Location of Inkbird IBS-TH1 Facade sensor relative to the entrance of the tomb (left). The weather station was placed inside an insert within the filling material of open fracture along the exterior of the façade wall (right).

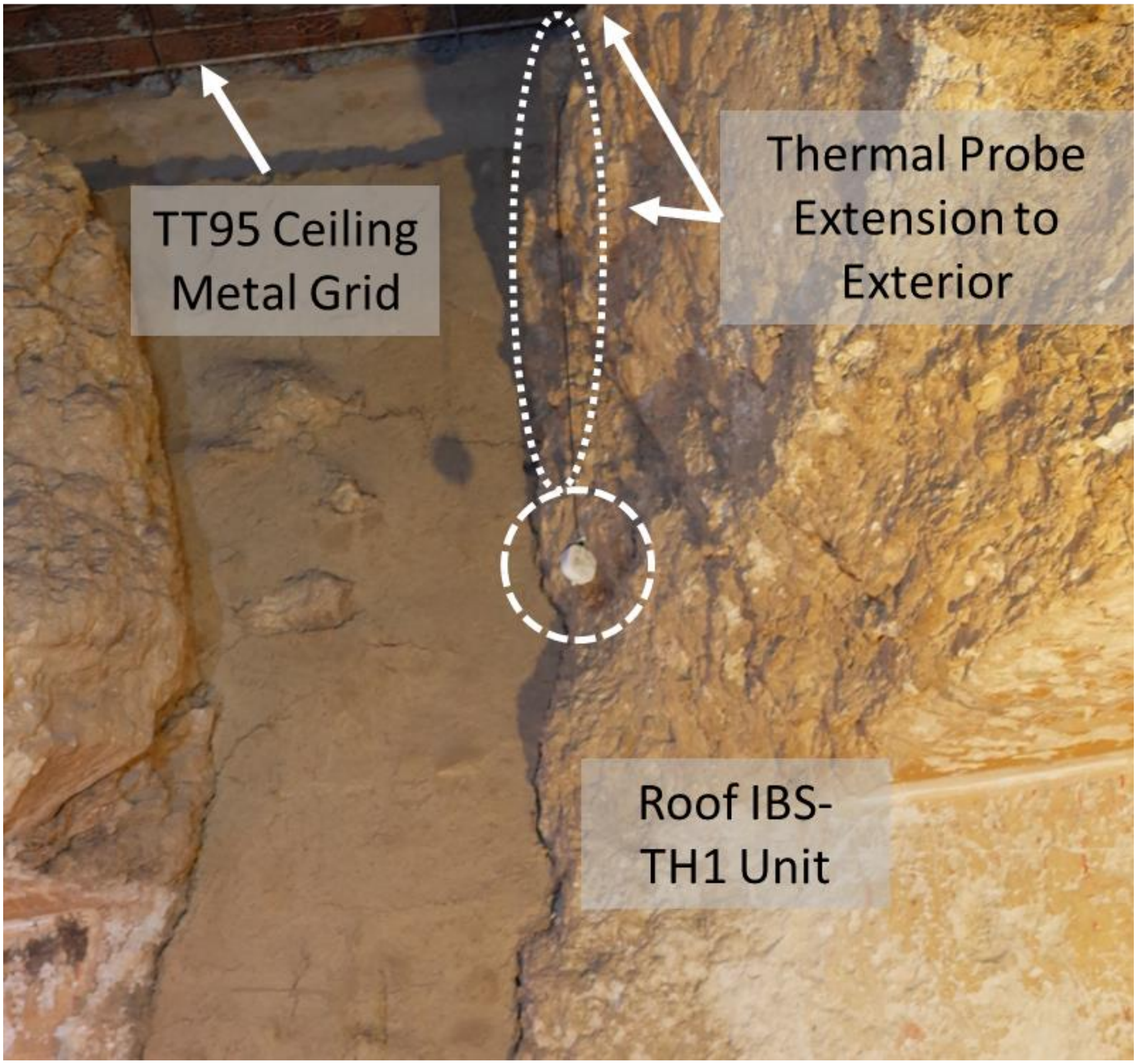

Figure 19: Inkbird IBS-TH1 sensor suspended by the metal grid covering the void space on the ceiling. The cable the sensor is suspended from is an extension probe for the device's thermometer. The probe is attached to an opening on the metal grid and records exterior ambient temperature measurements on the ceiling.

3.2 Exploratory Data Analysis (EDA)

The collected raw data were processed using the Python general programming language and the popular data analysis, plotting and statistical packages Pandas, Matplotlib, NumPy, SkLearn and SciPy [31], [32], [33], [34], [35], [36]. The EDA was the final step of the pipeline that starts at collecting and storing data locally

To draw insights from the data, the raw sensor feeds time series were plotted for all the instruments and analyzed for identifying abnormalities in the sensor output trends. Summary statistics were created for each of the sensor trends and analyzed for gaining insight into the range and measures of tendency and variance of the collected data.

A correlation analysis was conducted to find trends between sensors that correlate well with each other. The correlation analysis intends to find similarities between trends of the sensors measuring environmental parameters and the extensometer displacements. The correlation analysis in this study compares the Pearson R correlation of each sensor timeseries with each other.

3.3 Data Driven Modelling of Pillar Displacements

To answer the question of how the environmental trends affect the behaviour of the rock mass in TT95, as captured by the measured displacements by the extensometers, a supervised ML approach was developed. This chapter describes in detail how ML was used as a tool to determine two important factors that affect the measured extensometer displacements: a) which environmental parameters are the most important predictors of the extensometer displacements, and b) which timeframe is considered to be significant in terms of how long it takes for a particular environmental variable to produce an observed displacement capture by the extensometers.

3.3.1 Model Inputs and Grid Search of Best Predictors

The dataset used in this experiment consists of a collection of the instrument time series of measurements. Since the goal of this study is to examine how the rock responds to variations in temperature and humidity, the extensometer future displacements are of interest to forecast through the model, and the extensometer apertures were selected as the output variable, or “labelled” dataset for the model.

A grid search method was developed to discover which of the time series measurements, or which combination of them, are better predictors for the output variables. In this method, the grid refers to a matrix combination of the different input variable sets. The different input sets were created by combining and permuting through the sensor feeds together, grouping them based on what is the environmental parameter they measure (temperature and humidity input sets – interior and exterior). The previous aperture history was an additional input feed that was considered.

The second goal of the study is to also examine if there is a temporal aspect that plays a role in forecasting the future displacements. Are changes in displacements a result of short-term changes in temperature or is the observed behaviour a consequence of a longer-term process? The introduction of the temporal aspect as an additional input to the model was achieved by varying the range of the input time series that was passed as input to the model.

As such, the grid of input combinations was created by setting different combinations of sensor feeds as input sets on the matrix rows, with different time windows of the number of observations to be considered as a single data point. A group of models with identical architectures and hyperparameters would be trained on each of the individual input set-time window combination (grid entry). Each model performance would then be evaluated against a metric, in this case, based on the coefficient of determination (R^2) score of the forecasted dataset against the ground truth series, and compared against the rest of the models, with the hypothesis that the input set-timeframe combination of the best performing model are the best predictors for the observed displacements. The input grid used in this study is shown on Table 1.

3.3.2 Data Preprocessing and Measurement Synchronization

Gaps in the data arose due to power supply issues or memory capacity exceedance. To ensure the data were suitable for ML models, periods with missing values were removed. Only data points where all instruments recorded measurements concurrently were retained, resulting in a clean and uniform dataset. Additionally, differences in installation times, power interruptions, and recording intervals led to asynchrony in the data. To address this, all sensor measurements were resampled to 1-hour intervals. Resampling on temperature and humidity measurements was achieved by using the average measurements within a single hour interval, while extensometer aperture values used the sum of displacements within an hour. This synchronization facilitated the time series processing required for the CNN models.

Table 1: Input set grid, along with model names representing the input set used for each model (models for extensometer 1 end in _e1 suffix, while models for extensometer 2 end in _e2 suffix. The abbreviations of t, h and a correspond to inputs using temperature, humidity and aperture history respectively.)

Loockback Time (hours) Timeccck		AT	RH	AT-EA	RH-EA	AT-RH-EA
		AT – Ext. 1 AT – Ext. 2 AT – Roof AT - Façade	RH – Roof RH – Facade	All AT sensors & Extensometer History	All RH sensors & Extensometer History	All AT sensors & All RH sensors & Extensometer History
	12	12_t_e1 12_t_e2	12_h_e1 12_h_e2	12_ta_e1 12_ta_e2	12_ah_e1 12_ah_e2	12_tha_e1 12_tha_e2
	48	48_t_e1 48_t_e2	48_h_e1 48_h_e2	48_ta_e1 48_ta_e2	48_ah_e1 48_ah_e2	48_tha_e1 48_tha_e2
	168	168_t_e1 168_t_e2	168_h_e1 168_h_e2	168_ta_e1 168_ta_e2	168_ah_e1 168_ah_e2	168_tha_e1 168_tha_e2

3.3.3 Model training

Model training is the process of updating the model weights and biases by feeding it a set of labeled samples. A portion of the entire clean dataset is reserved for training the model, while the rest is kept for evaluating its performance.

The model's weights and biases are initially randomly assigned. A prediction is made by feeding the sample input vector to the CNN model. The prediction is then compared to the real output from the sample, taken from the training data subset, whose difference is the error of the prediction. The training algorithm is then using the error value to update the weights and biases of the model, attempting to minimize the error.

Model training is controlled by a number of variables that are called hyperparameters of the model. Hyperparameters control the learning process of the model and are used to reduce overfitting and increase the reliability of the model predictions and thus the trust to the model.

3.3.4 Data splitting, scaling and shuffling

The data were split into two sets, a set reserved for training of the models, and a set reserved for evaluating the model performance, the forecasting set. The training set consisted of measurement data from April 9, 2019, up to January 1st, 2023. Sensor data from January 1st of 2023 to March 1st, 2023, were making up the forecasting set.

To deal with any inconsistencies between the ranges of the input variables, all sensor measurements were scaled on the interval between 0 and 1. Scaling of the dataset is a typical process in the data-driven development process as it facilitates updating the weights of the CNN in error backpropagation, during model training [37].

The training set was divided into 2 sets during training, one for the actual training of the model and one validation dataset, to evaluate the model performance during training. The validation dataset contained 20% of randomly selected data points from the training dataset. The 80% of the final training dataset was then randomly shuffled to introduce randomness on the training process and reduce overfitting.

3.3.5 Loss function

The role of the loss function is to quantify the error between the model predictions and target measurements. The model learning process utilizes the error calculated by the loss function and uses it to adjust its weights and biases with the aim of minimizing that error in subsequent model predictions. Selecting an appropriate loss function for training a model depends mainly on the type of problem at hand (classification vs regression) as well as the type of variables that are being used (categorical vs numerical). There are also instances where selecting the best possible loss function is not clear before training a model and examining the residuals and their distribution.

The collected dataset from the instrumentation in TT95 is solely in numerical format, and the type of problem falls into the regression category, as the goal is to make future predictions about the future extensometer displacements. Thus, the loss function selected for training the extensometer models was a mean absolute error function:

$$MAE = \frac{\sum_{i=1}^{n} |\hat{y}_i - y_i|}{n}$$

Where

- $\hat{y}_i$: forecasted value
- y_i: real value
- n: number of observations

Number of Epochs

Number of epochs is a hyperparameter that controls overfitting and refers to the number of times the training dataset is passed to model for updating its weights and biases. At the end of each epoch, the model has adjusted its weights and biases to reduce the overall prediction error. Thus, after the model has seen the input dataset at least once, it has probably become a better model than one with randomly assigned weights and biases. If the model training process runs smoothly, the model performance is expected to improve after each epoch, until it reaches a plateau where the best fit for the data has been determined for that model. After the plateau is reached, no improvement in performance can be made by increasing the number of epochs.

A good process for finding the most optimal number of epochs, is to identify that plateau in performance by plotting the model loss after each epoch. When the model loss stops decreasing after a certain number of epochs, the model has reached its best performance. This, however, does not mean a good model has been found. It simply means that further training iterations will provide diminishing returns in terms performance, and computational resources could be utilized in finding a better model by different means than solely running more epochs.

3.3.6 Model Architecture

The model architecture for the CNN models used in this study is generic and serves as a starting point for optimizing the model architecture in future research. An overview of the selected architecture is shown in Figure 19.

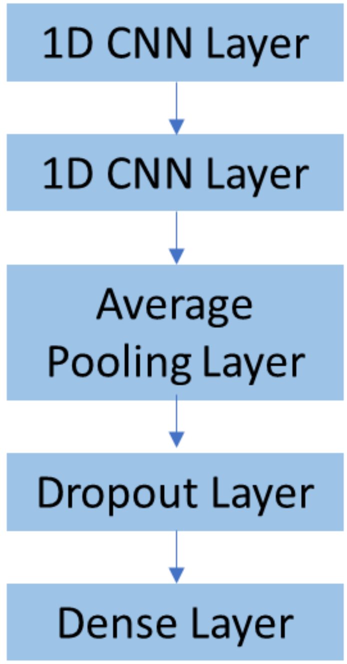

Figure 20: CNN model architecture used in this study

The model architecture consists of 2 stacked, 1-dimensional convolutional layers, with 64 and 32 filters respectively, a kernel size of 3 and ReLU (Rectified Linear Unit) activation. An average pooling layer prepares the output of the filters to feed a dropout layer, which randomly turns off half of the layer's neurons (0 activation) in each epoch, to introduce randomness to the training process and reduce overfitting. The last layer of the network is a fully connected layer, with a sigmoid activation to wrap up the network architecture and map the output to a single numerical value.

3.3.7 Model Evaluation and Performance

After training, the models will be used for making displacement forecasts using the evaluation dataset as input. The forecasted values of extensometer displacements were compared against the true observed extensometer displacements and the model performance was evaluated by using a metric that quantifies how close the forecasted displacement trend, to the observed trend. The metric used were the coefficient of determination, or R^2 score:

$$R^2 = 1 - \frac{Sum\ of\ Squared\ Regression}{Total\ Sum\ of\ Squares} = 1 - \frac{\sum(y_i - \hat{y}_i)^2}{\sum(y_i - \bar{y}_i)^2}$$

4 RESULTS AND ANALYSIS

4.1 RAW SENSOR DATA

The choice of an appropriate methodology for processing and analyzing that collected data is partially dependent of the type of data that are being collected. Sensor measurements are typically stored in a time-series, where every collected measurement is associated with a timestamp of when it was collected. In time-series analysis, the temporal component of the data adds to the complexity of the analysis, both at the preprocessing level and at the interpretation of results level. The next subsections give an overview of the raw collected data from the sensors of the monitoring equipment.

4.1.1 Range of data collected, and sensors omitted from the study

Measurements from the extensometer displacements and the Inkbird sensors commenced on April 9 of 2019. Due to battery and logger memory capacity issues, the stream of measurements ended on July 15 of 2019, for the extensometers, October 20, 2019, for the Inkbird sensor on the façade, and April 19, 2020 for the Inkbird sensor installed on the ceiling. The data collection for all instruments begun again in March 10, 2022, with a subsequent site visit where maintenance of the monitoring system was performed. The antenna of the extensometer 2 which was transmitting data to its logger got damaged and extensometer 2 data collection was not restored during the site visit. Extensometer 1 data was collected until the end of June of 2022, where memory limitation impeded the data collection again. The extensometer operation started again in August of 2022 in a subsequent site visit and data collection was improved by adding the Raspberry Pi module to the system setup, which solved the memory capacity and battery power supply issues experienced before. The last site visit was performed in March of 2023, which provided the last opportunity for retrieving data collected from the Inkbird Bluetooth sensors. Upon a preliminary examination of the raw sensor readings, the temperature and humidity measurements obtained from the Arduino setup had a lot more noise and variance than those obtained from the Inkbrid sensors. This inconcistency could be the result of difference in instrument precision, or a damage in the monitoring setup which either occurred past the site visit in 2023, or a different factor that played a role in adding noise to the measurements (quality and length of cables used to connect the sensors to the Arduino board). To mitigate this this study used the available data from April 2019 to March 1st, 2023 and climatic data past that date (data from the Arduino sensors) were not presented. However, the available data for the extensometer measurements past March 2023, until November 2023 are included since they were not affected by this issue. Figure 21 below shows a summary of the date ranges with available data, for the sensors used in the study.

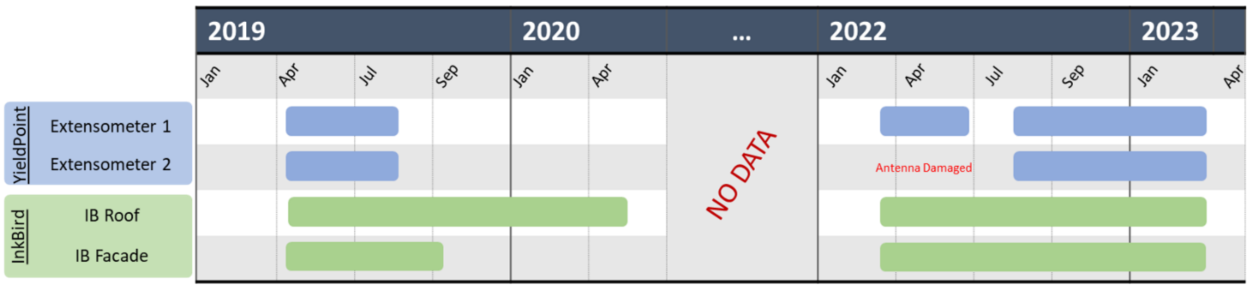

Figure 21: Date ranges of collected data.

4.1.2 Ambient Air Temperature

Figure 22 shows plots of the time-series measurements collected by each of the temperature sensors. The roof and façade sensors measured a mean temperature of 34.1^0C and 32.4^0C, respectively. A mean temperature of that level is characteristic of the warm climate in the area, as summarized in Table 2. The minimum temperature recorded was 14.4^0C, with a max temperature reaching as high as 47^0C since recording began in 2019. It's important to note that the range of temperatures recorded within the monitoring period, combined with the lack of precipitation within the same period assert that the rock mass is not exposed to any freeze-thaw cycles nor any water-based damage mechanisms (swelling etc.), which helps focus this study on thermal or humidity driven damage.

Mean daily variation for exterior temperatures were measured at 9.6^0C from the roof sensor and at 6.3^0C from the one in the façade. The discrepancies between the two instruments can be attributed to the location of the sensors. The roof sensor is placed in close proximity to a metal grid that is being used to cover the opening on the ceiling. The façade sensor is placed inside a small hole in the façade. The façade is exposed to direct sunlight much less than the ceiling due to shadows cast by the tomb in the afternoon hours. Additionally, the metal grid conducts and dissipates heat faster than the rock, which explains the greater variability in intraday fluctuations and the higher maximum temperature reading.

Interior temperatures remain much more stable, with a temperature difference never exceeding 10^0C in the entire monitoring period, and an average intraday temperature fluctuation of less than 1^0C.

Table 2: Summary of temperature measurements

	Extensometer 1 (Interior Air Temperature)	**Extensometer 2 (Interior Air Temperature)**	**Roof Thermometer (Exterior Air Temperature)**	**Façade Thermometer (Exterior Air Temperature)**
Mean (^{0}C)	29.1	29.1	34.1	32.4
Min (^{0}C)	23.5	23.8	17.7	14.4
Max (^{0}C)	33.5	33.1	47.0	45.7
Range (^{0}C)	10.0	9.3	29.3	31.3
Mean Intraday Range (^{0}C)	0.3	0.3	9.6	6.3
Min Intraday Range (^{0}C)	0.0	0.0	0.7	1.7
Max Intraday Range (^{0}C)	1.4	1.2	15.9	11.7

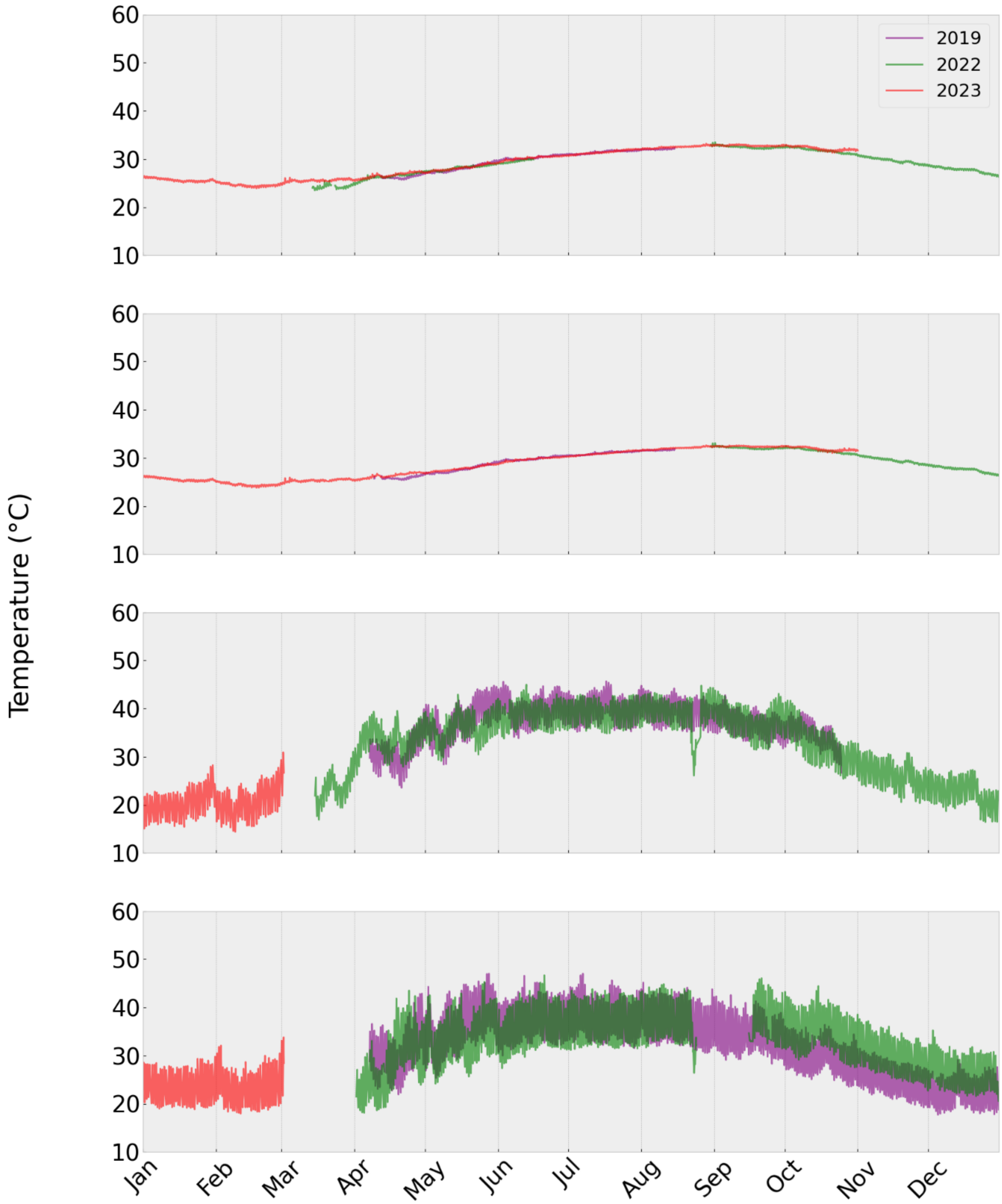

Figure 22: Air temperature time-series collected by each temperature sensor (Order from top: Extensometer 1, Extensometer 2, Façade sensor, ceiling sensor).

4.1.3 Relative Humidity

Ambient relative humidity levels range from 1% to 47%, with a mean humidity level of 20% and an average intraday range of 8.1%. Such low humidity levels are characteristic of arid and desert climates. The interior of the tomb maintains an average humidity level of 18.9% with average daily fluctuation of 3%. This low variation in the interior humidity combined with the low variation of the interior temperature shows that the tomb is well insulated from ambient conditions.

Table 3: Summary of Humidity Measurements

	Roof Hygrometer (Interior Relative Humidity)	**Façade Hygrometer (Exterior Relative Humidity)**
Mean (%RH)	18.9	20.0
Min (%RH)	8.0	1.0
Max (%RH)	41.2	47.0
Range (%RH)	33.2	46.2
Mean Daily Range (%RH)	3.0	8.1
Min Daily Range (%RH)	0.4	1.4
Max Daily Range (%RH)	15.9	21.3

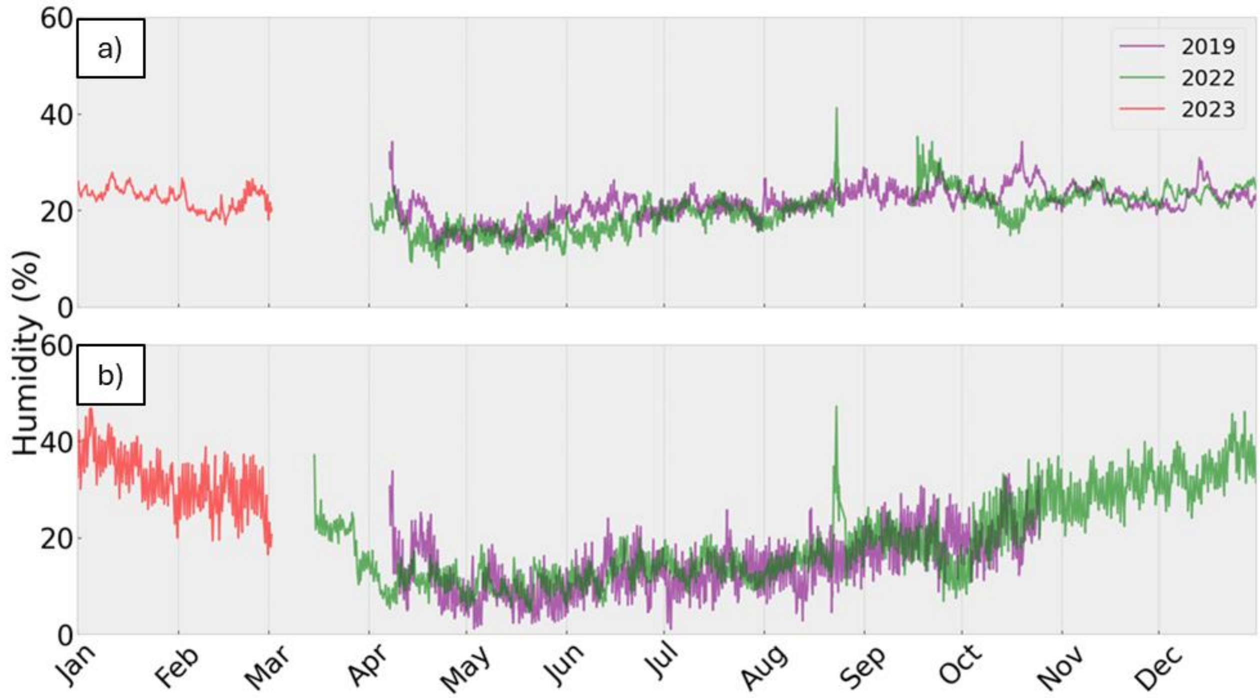

Figure 23: Time series of relative humidity measurements from hygrometers: a) roof hygrometer (interior humidity), b) façade hygrometer (exterior humidity)

4.1.4 Extensometer Displacements

Since the extensometers installed in TT95 output the instruments aperture, the instrument displacements were used to monitor the movements of the critical pillar. The displacements of the extensometers were defined as the difference between the current extensometer aperture and the first recorded aperture which was arbitrarily set at time of installation.

The observed displacements were in a range of a few tenths of a millimeter for both extensometers (Figure 24), with Extensometer 1 exhibiting a slightly higher range of displacements. Both extensometers showed seasonal trends with high positive displacements occurring during the colder months and low negative displacements during the warmer months. Summary statistics for the extensometers are summarized in Table 4 below.

Table 4: Summary of extensometer displacement measurements

	Extensometer 1	Extensometer 2
Apperture @ Point 0 (μm)	*5088.0 @ 9 Apr. 2019 12:00:00*	*4096.0 @ 9 Apr. 2019 12:00:00*
Min (μm)	-254.0	-187.0
Max (μm)	170.0	209.7
Range (μm)	424.0	396.7
Mean Daily Range (μm)	4.2	4.2
Min Daily Range (μm)	0	0
Max Daily Range (μm)	26.0	53.2

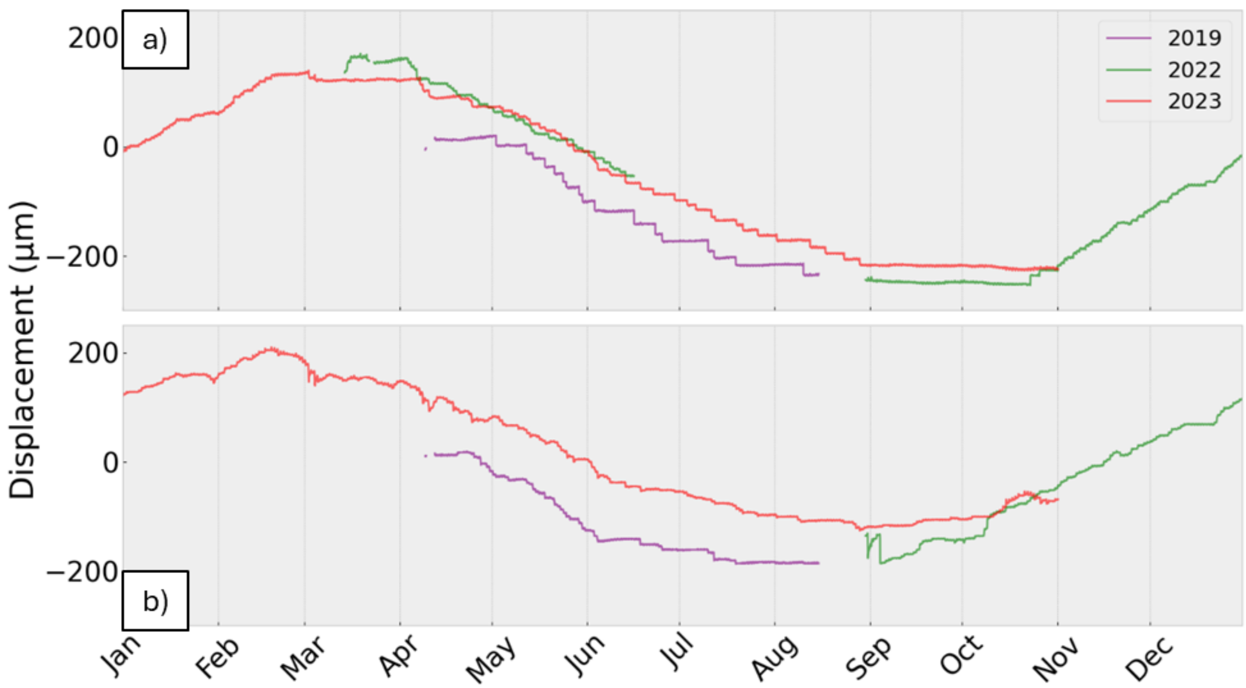

Figure 24: Time series of extensometer displacement measurements: a) Extensometer 1, b) Extensometer 2 (Notes: Time start of measurement is in April 2019; The bump in the extensometer displacement observed in the beginning of September of 2022 is a known disturbance to the sensor and is not related to any physical movement of the rock)

4.2 Correlation Analysis

The table below (Table 4) presents the Pearson correlation matrix for each collected measurement time-series in relation to the others. Notably, interior air temperatures exhibit a positive correlation with exterior ambient temperatures. Exterior temperatures also display correlations ranging from mild to strong with exterior humidities. Additionally, interior temperatures demonstrate a very strong negative correlation with extensometer displacement time series, which in turn exhibit correlations ranging from mild to strong with exterior temperatures. However, humidity series demonstrate very weak correlations with extensometer displacements.

Table 5: Correlation analysis results. Each entry of the grid is the Pearson-R correlation value between the time series of the sensor in the same row with the sensor of the same column.

	Interior Air Temp. (EXT1)	Interior Air Temp. (EXT2)	Exterior Air Temp. (Ceiling)	Exterior Air Temp.	Exterior Humidity (Façade)	Interior Humidity (Ceiling)	EXT1 Disp.	EXT2 Disp.
Interior Air Temp. (EXT1)	**1.00**	**1.00**	**0.64**	**0.67**	**-0.30**	**0.23**	**-0.93**	**-0.92**
Interior Air Temp. (EXT2)		**1.00**	**0.61**	**0.64**	**-0.26**	**0.25**	**-0.95**	**-0.91**
Exterior Air Temp. (Ceiling)			**1.00**	**0.82**	**-0.60**	**-0.14**	**-0.47**	**-0.68**
Exterior Air Temp. (Facade)				**1.00**	**-0.82**	**-0.22**	**-0.46**	**-0.79**
Exterior Humidity (Façade)					**1.00**	**0.53**	**0.07**	**0.50**
Interior Humidity (Ceiling)						**1.00**	**-0.47**	**-0.19**
EXT1 Disp.							**1.00**	**0.86**
EXT2 Disp.								**1.00**

The significant inverse correlation between interior temperature and extensometer displacement provide compelling evidence that periodic temperature fluctuations induce micromovements within the rock mass, as captured by the extensometers. Throughout the majority of the year, the tomb entrance remains closed, devoid of archaeological activity or site visits. Consequently, air circulation within the tomb is minimal to negligible, effectively rendering the tomb a sealed chamber. The fluctuations in interior temperature stem from a heating process directly influenced by ambient temperature trends. Ambient air temperature and solar radiation impart heat to the rock mass, which then conducts this heat to warm the interior ambient air.

Initially, the weak correlations between exterior temperature and extensometer displacements may not robustly support the hypothesis that ambient temperature fluctuations drive the observed displacements. However, it's noteworthy that weak correlations are also observed between interior and exterior temperature readings. Given the absence of alternative mechanisms for heating the tomb's interior, this weak correlation might be attributable to the lag created by the time required for heat to permeate through the rock mass and warm up the interior air.

4.3 Pillar Displacements

The orthogonal and coplanar placement of the extensometers on the adjacent faces of pillar K enables tracking of the centroid movement of the pillar over time within the plane of their installation.

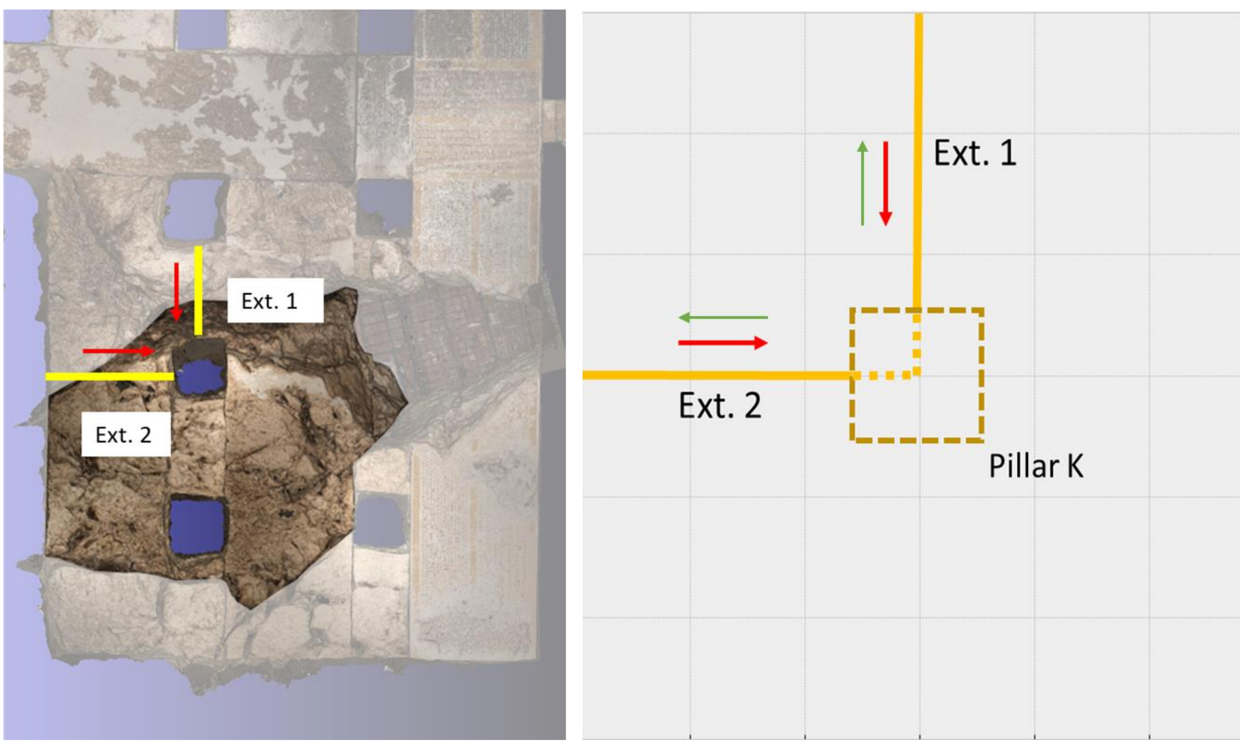

Figure 25: Extensometer position relative to isolated ceiling block (left). Extensometers 1 and 2 are install orthogonally on the North and West faces of Pillar K. Positive displacement values denote extensometer expansion, while negative displacements signify instrument contraction.

It's crucial to acknowledge that the movements recorded by extensometers 1 and 2 are relative to adjacent pillar J and the west wall, respectively. They do not facilitate tracking of absolute displacement from a fixed point of reference. Upon visual inspection of the fracture network along the ceilings, it becomes evident that pillars K and L support a block surrounded by open fractures. Additionally, pillar J does not exhibit a reduced cross-section like that observed on the top of pillar K, nor does it show any signs of structural damage.

These observations are instrumental in making the critical assumption that the west wall and pillar J are considerably stiffer than pillar K, thus serving as fixed points of reference for tracking the movement of pillar K. Furthermore, since both extensometers intersect the fracture plane, movements in pillar K could offer insights into the relative movements between the isolated block supported by pillars K and L and the surrounding rock mass.

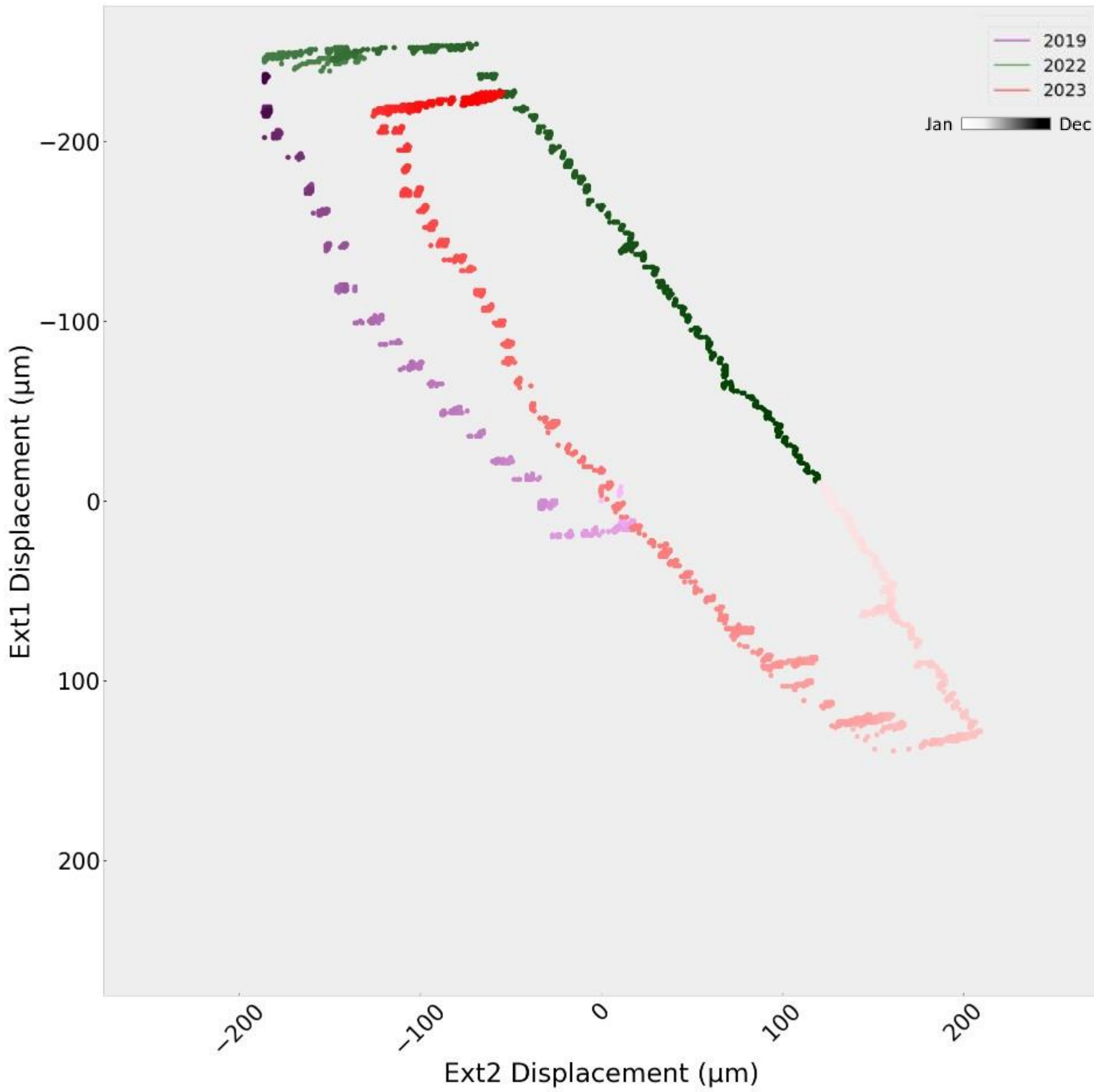

Figure 26: Combined displacement plot for both extensometers. The points on the plot represent the position vector of the resultant displacement over time. Darker shades represent late time within the year

Figure 26 depicts the trace of the displacement vector resulting from the combination of the two extensometers. The y-axis is inverted to align the plot with the plan view of pillar K, as illustrated in Figure 25.

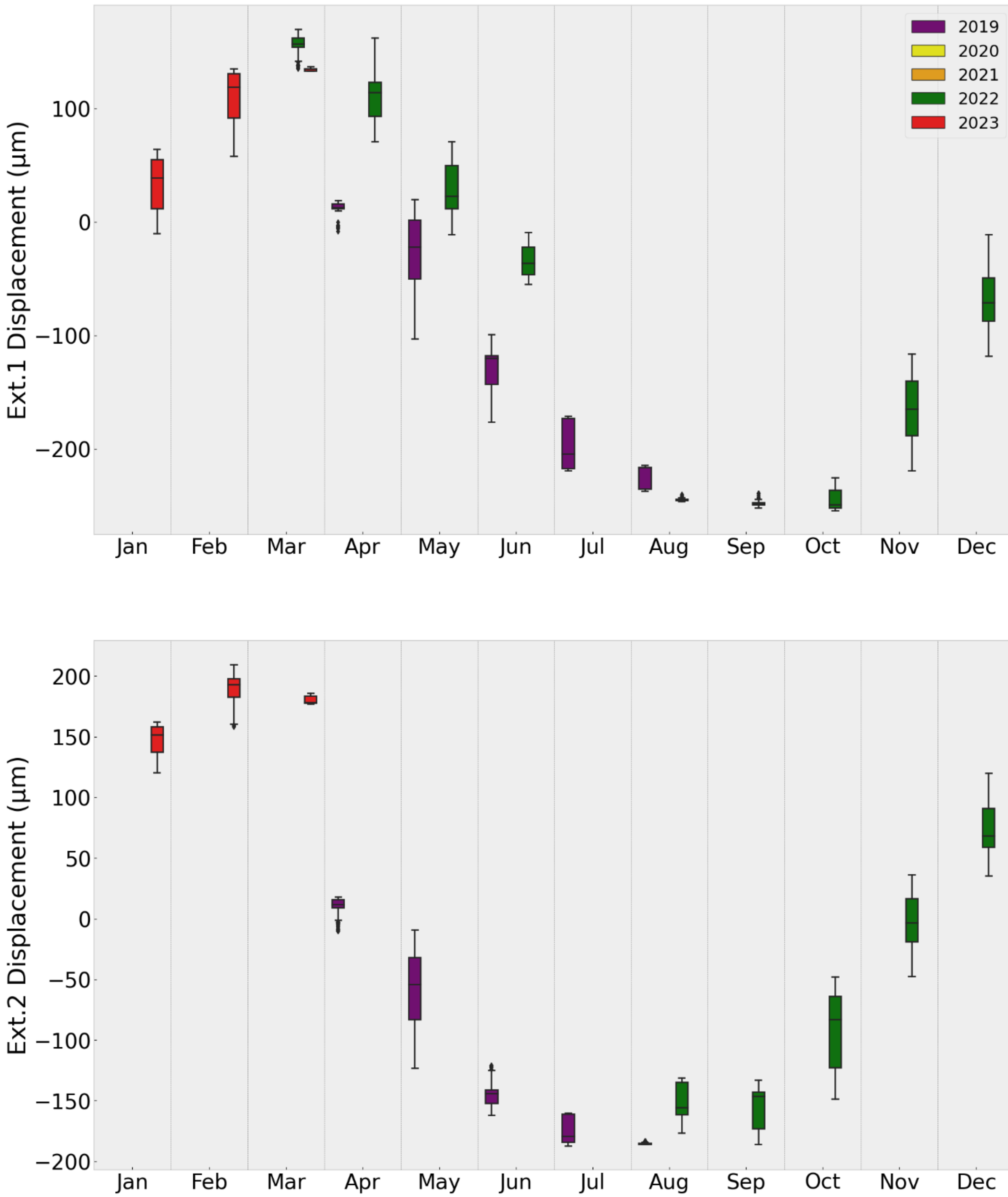

Figure 27: Box plots summarizing the monthly extensometer displacement range for extensometer 1 (top) and 2 (bottom).

The end of the plateau signifies the commencement of the cooling period (October – February), characterized by a shift in ambient air temperatures from the year's highs to colder temperatures. During this cooling phase, the extensometers expand. Following the cooling period are the yearly lows and the winter plateau, which, in turn, precede the trend reversal, thus repeating the observed yearly pattern.

In the heating period, rising temperatures heat the rock, resulting in thermal expansion and an increase in volume. Throughout the plateau periods, temperature fluctuations are confined to small, consistent daily variations, maintaining the rock at a relatively constant temperature for a period. Consequently, the volume remains constant during this time. As the rock cools down with decreasing temperatures, thermal contraction occurs, leading to a reduction in volume, thereby opening up the fractures. This cyclical process repeats itself over time.

	Extensometer 1	**Extensometer 2**	**Rock Mass**	**Fracture Aperture**
Cooling Period	Expands	Expands	Contracts	Opens
Winter Plateau	Negligible displacements	Small displacements	No volume change	No change in aperture
Heating Period	Contracts	Contracts	Expands	Closes
Summer Plateau	Negligible displacements	Small displacements	No volume change	No change in aperture

4.4 Effect Of Temperature On Pillar Displacements

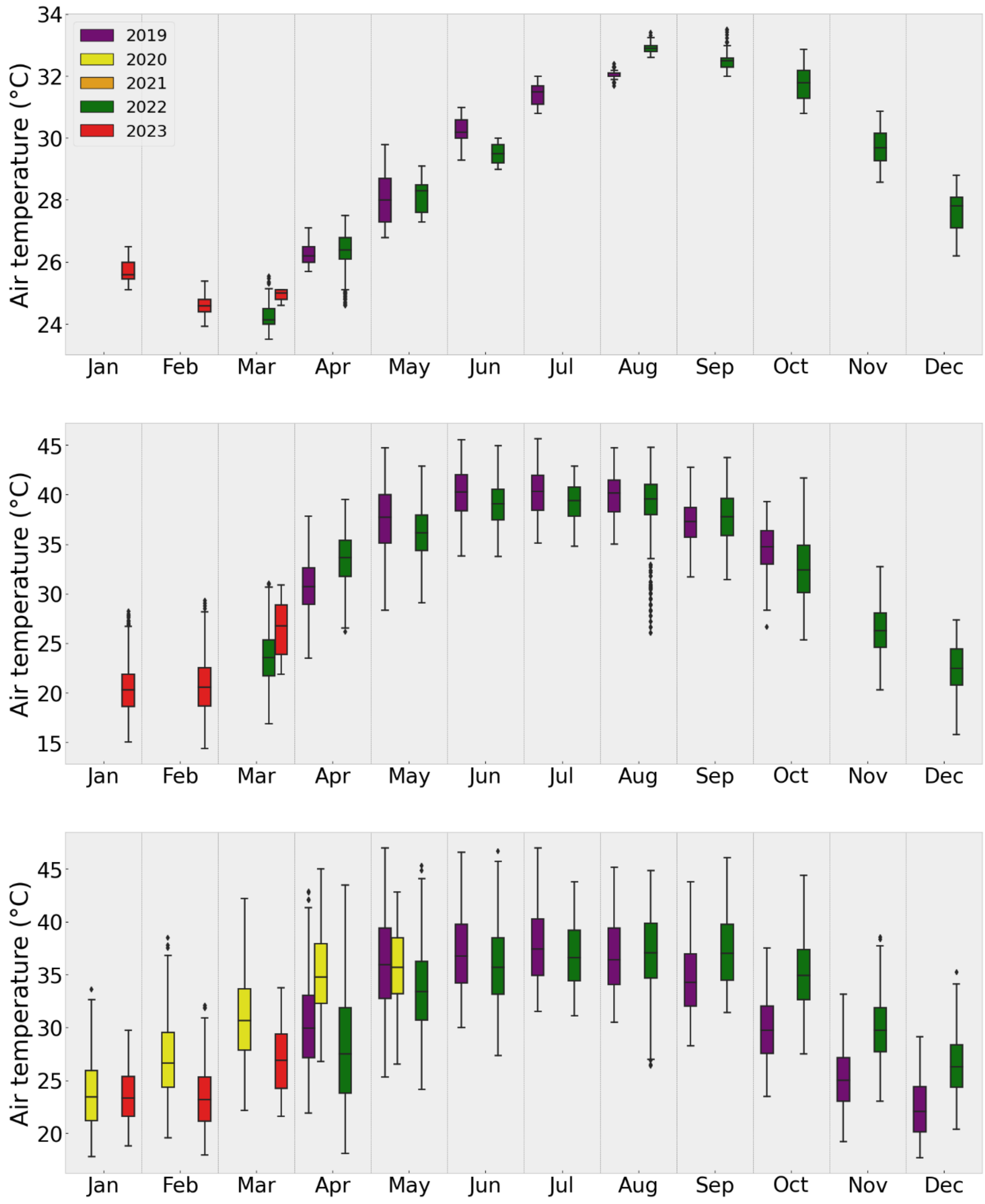

Figure 28: Boxplots indicating the range of monthly temperatures (Top: Interior extensometer temperature, middle: exterior facade temperature, bottom: exterior ceiling temperature)

The boxplots presented above (Figure 28) illustrate the monthly range of temperature measurements for each year with available data. The shorter range depicted in the first boxplot indicates the considerably smaller magnitude of temperature measurements from the tomb interior, characterized by minimal daily deviations and a distinct seasonal trend. In contrast, the boxplots of the exterior extensometers reflect noisier temperature signals from those sensors, capturing larger daily fluctuations and a less clearly defined seasonal pattern, albeit still noticeable.

Figure 29 and Figure 30 depict plots of temperature measurements from each temperature sensor against the displacements of each extensometer. The extensometer movement range is delimited by the plateaus formed near the minimum and maximum temperatures of each year. A linear relationship is discernible between the interior air temperature of the tomb and the extensometer displacements between the plateaus, completing a cycle as temperatures fluctuate seasonally each year.

The end of the plateau marks the onset of the cooling period, during which the ambient air temperature transitions from the year's highs to colder temperatures. The drift of the extensometers observed in the preceding plot can also be observed in these temperature-displacement plots, as evidenced by the widening of the band bounded by the cooling and heating linear trends.

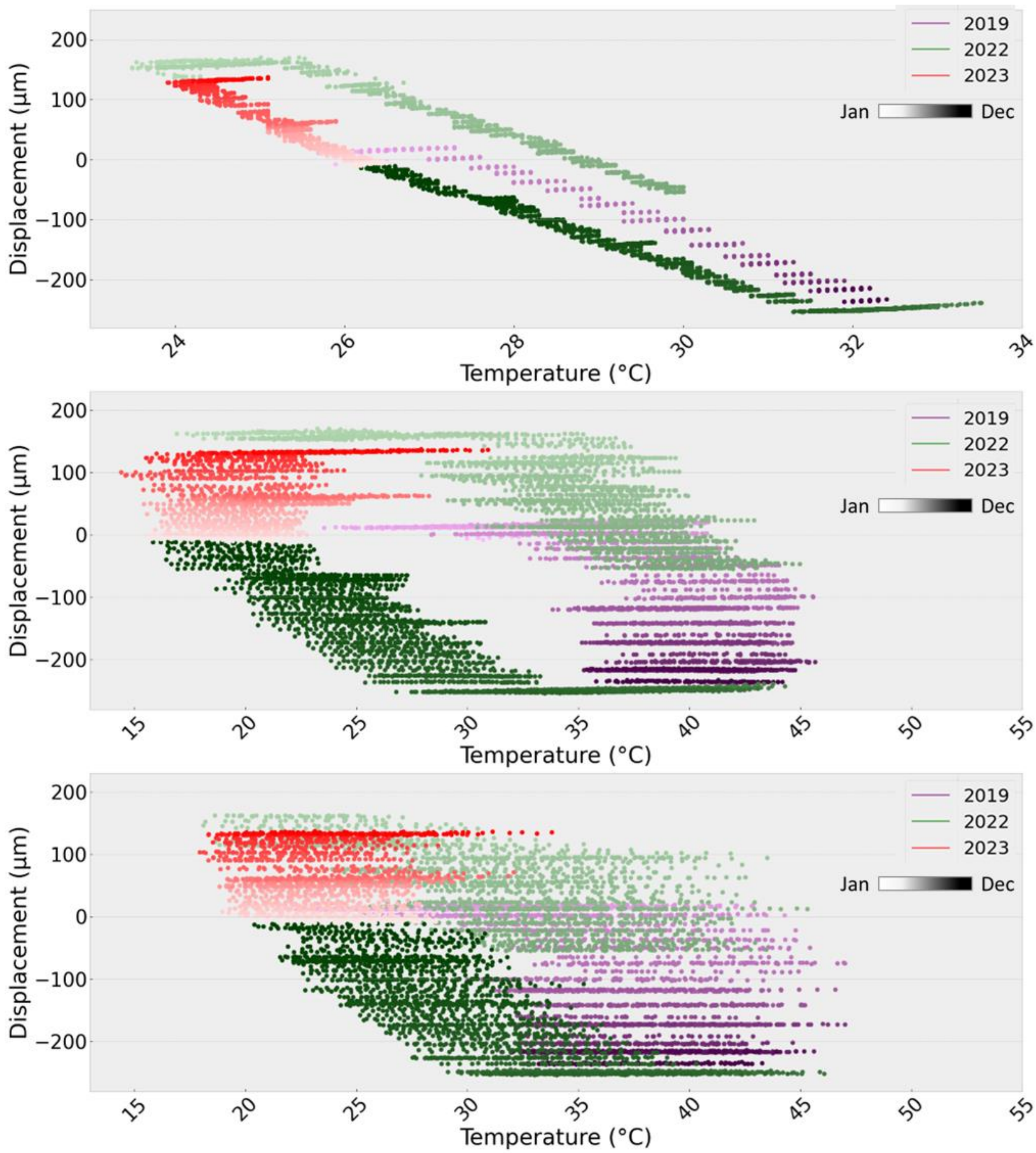

Figure 29: Plots of ambient air temperature measurements from each sensor against extensometer 1 displacements. (Top: interior air temperature from ext 1 sensor, middle: exterior air temperature at the façade, bottom: exterior air temperature at the ceiling).

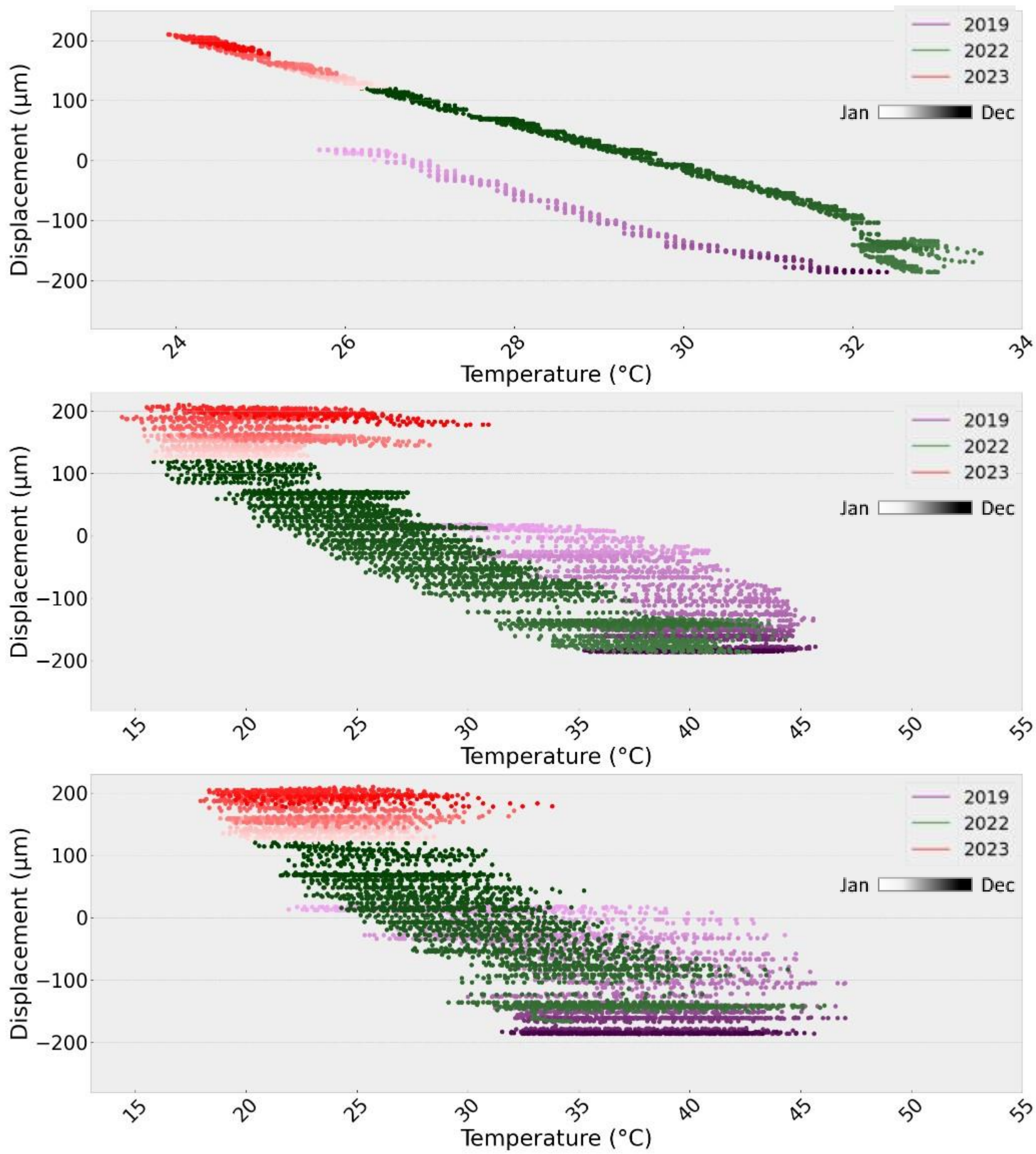

Figure 30: Plots of ambient air temperature measurements from each sensor against extensometer 2 displacements. (Top: interior air temperature from ext 1 sensor, middle: exterior air temperature at the façade, bottom: exterior air temperature at the ceiling).

However, the presence of gaps in measurements and issues with data access concerning the exterior temperature sensors after March 2023 make year-on-year comparisons challenging. A visual examination reveals that available 2019 data exhibited higher average temperatures than those recorded in 2022 and 2023, particularly between April and August, which are the only months with available 2019 data. Furthermore, 2023 emerged as a warmer year, boasting higher monthly averages than 2022, with the exception of the peak in August 2022. Notably, interior temperatures in early 2024 suggest a significantly warmer interior compared to a year prior, continuing from a notably warmer late 2023 (relative to 2022).

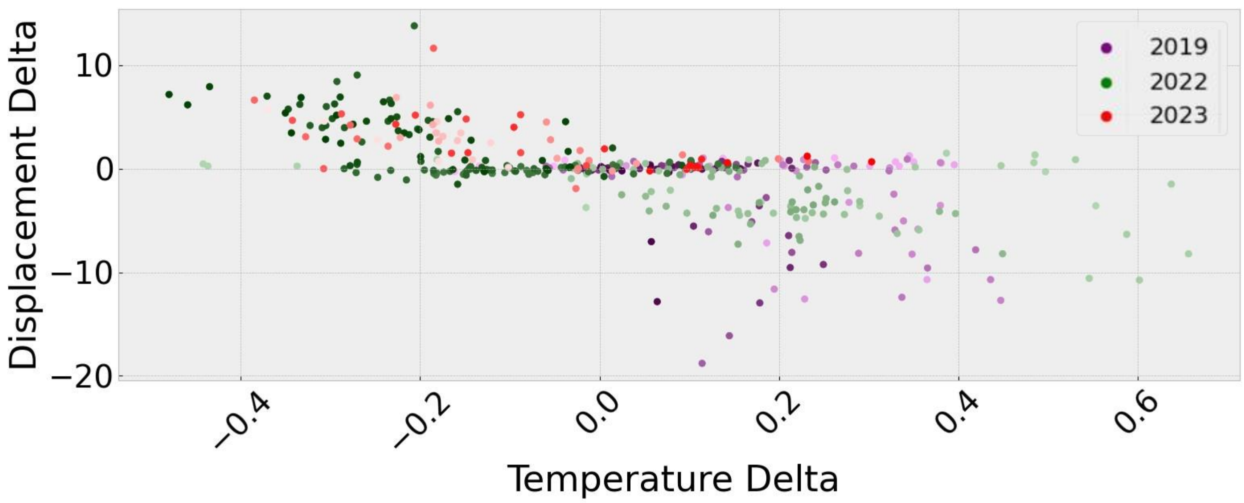

Figure 31: Plot of change in displacement with hourly change in interior air temperature.

The plot in Figure 31 illustrates the relationship between temperature changes and observed displacement magnitudes. It's noteworthy that large positive displacements correlate with decreasing temperatures, and conversely, negative displacements coincide with temperature increases.

The trace of the pillar displacement unveils an intriguing pattern. Throughout the heating period of each year (April-August; refer to Figure 27), as ambient air temperatures rise from winter lows, both extensometers contract. This contraction continues until reaching a plateau in September, during which both extensometers slow down significantly until the end of the plateau period.

4.5 Effect Of Humidity on Pillar Displacements

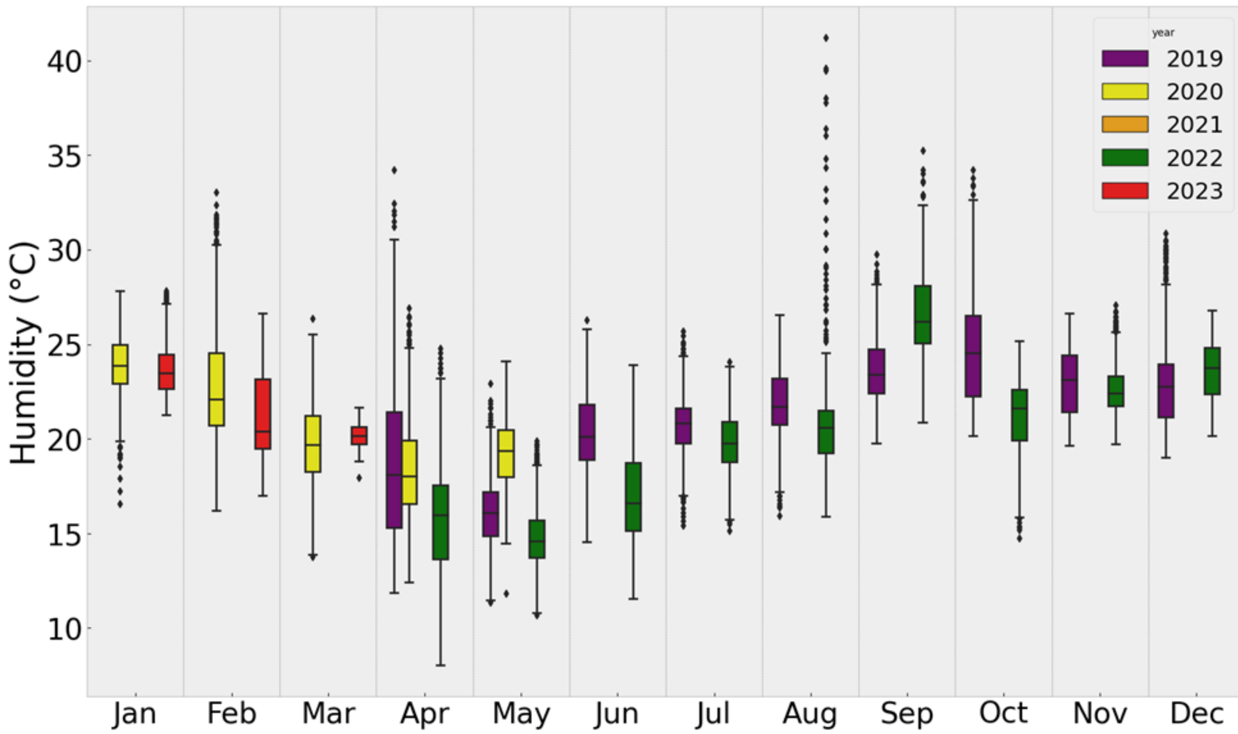

Figure 32: Boxplot of monthly interior ambient humidity ranges, grouped by year

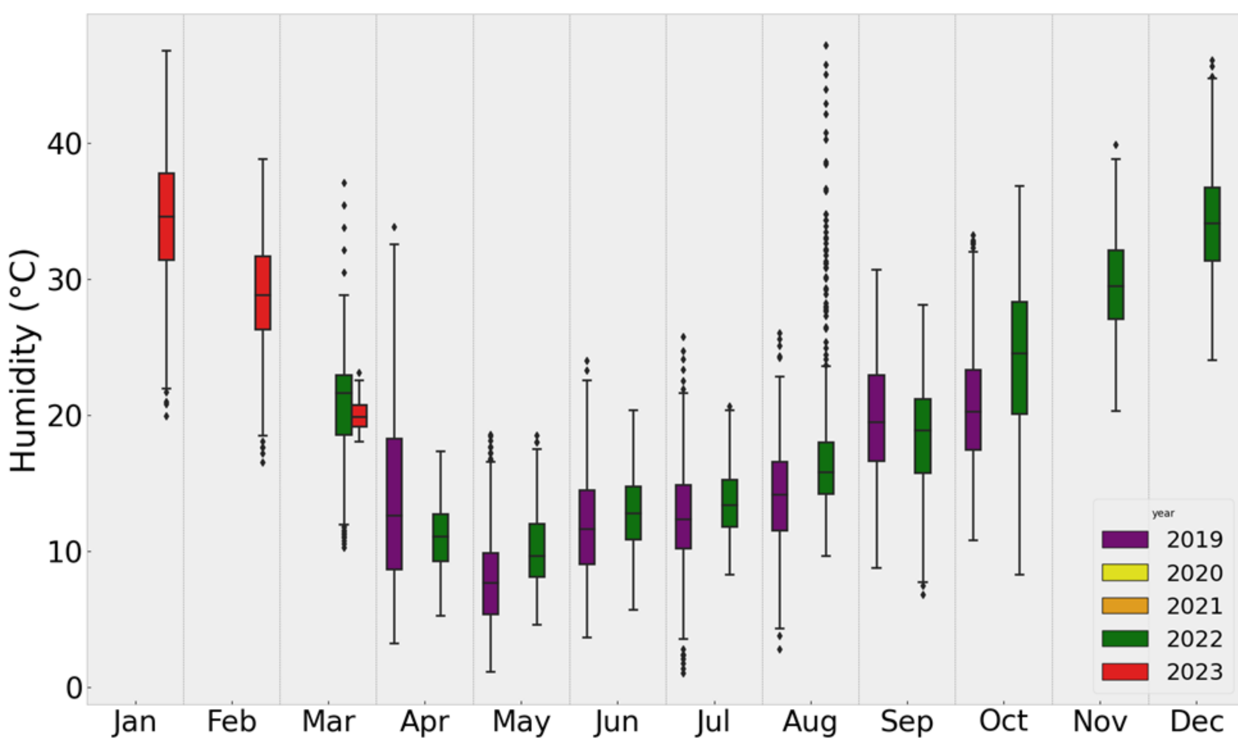

Figure 33: Boxplot of monthly exterior humidity ranges, grouped by year

In the above boxplots (Figure 32 and Figure 33) the monthly ranges of interior and exterior humidity measurements are shown. The interior humidity levels exhibit smaller variance but, unlike the interior temperature, the seasonal trend is less clear. The exterior humidity levels are generally higher than the interior in colder months whereas the opposite is true in warmer months. This is likely the result of minimal air circulation within the interior if the tomb and the fact that the tomb remains sealed during the year.

The humidity-extensometer displacement plots presented below (Figure 34) also reveal a cyclical pattern, albeit less pronounced than that of the temperature-displacement plots shown in the previous subsection, hinting that the effect of humidity on the extensometer displacements is less clear.

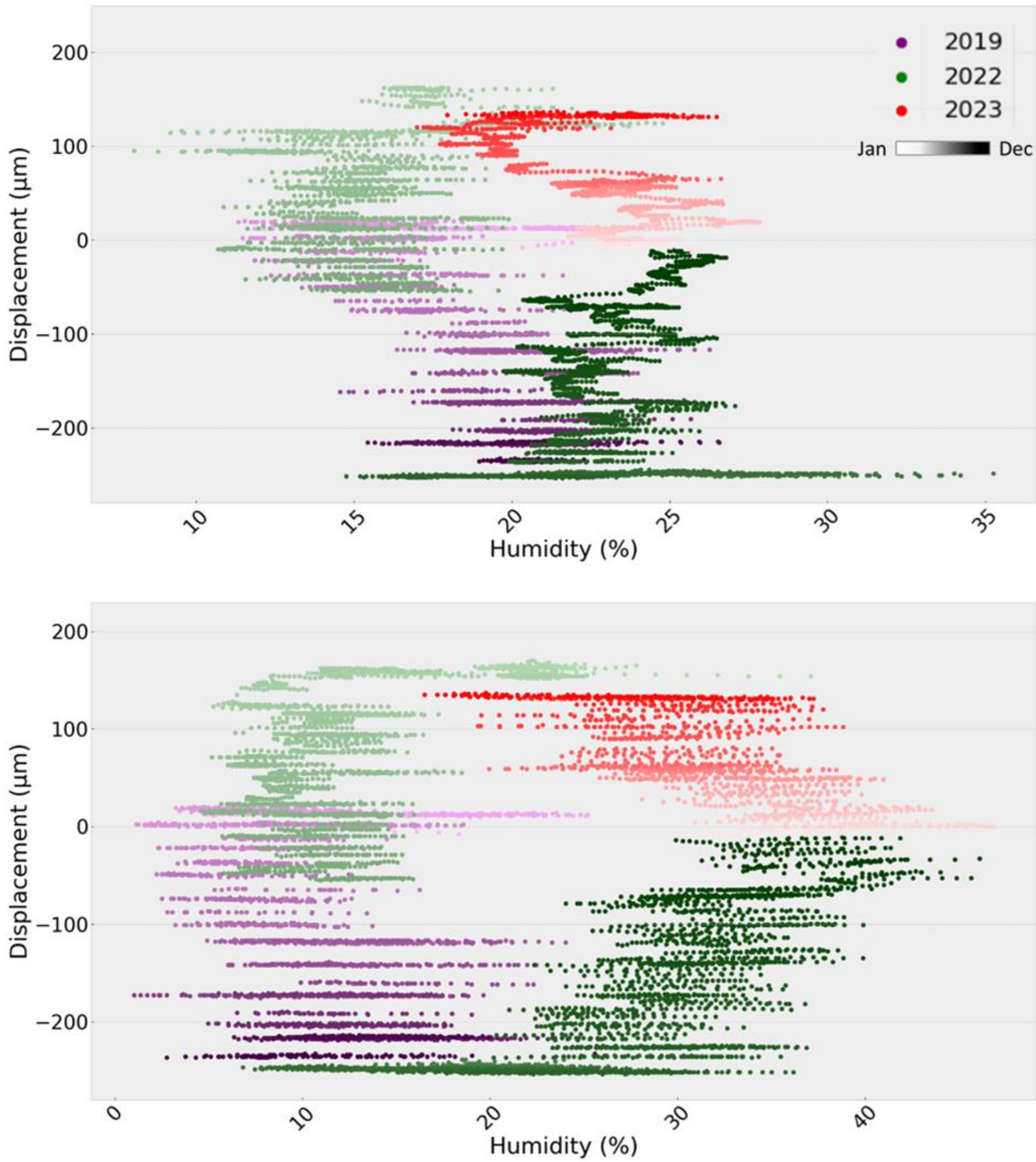

Figure 34: Plots of ambient relative humidity measurements from each sensor against extensometer 1 displacements. (Top: interior humidity from the roof Inkbird sensor , bottom: exterior humidity from façade Inkbird Sensor).

4.6 ML MODELING RESULTS

The subsections below contain a summary of the performance of the CNN models on the training, validation, and forecasting datasets.

4.6.1 Modeling Extensometer 1

Table 6 below shows a summary of the performance evaluation of the Extensometer 1 models. All models, with the exception of the models whose input was humidity, performed very well on the training and validation datasets as suggested by the high R^2 values (>0.95) and lower MSE (<1000). Models that did not include the previous extensometer aperture history as an input performed poorly on forecasting, with low R^2 values for the temperature models, and very low R^2 values for the humidity models. The models that included the extensometer history performed very well on the forecast dataset, with an R^2 value exceeding 0.95 for almost every single model, except the temperature-aperture model with a 12-hour lookback window. The best performing model was 12_tha_e1, which used temperature-humidity-aperture history as its inputs.

Table 6: Training, Validation Forecasting performance evaluations for Extensometer 1 CNN models

Model ID	Lookback Window (hrs.)	Input variables	Training R^2	Training MSE	Forecast R^2	Forecast MSE
12_t_e1	12	Temperature	0.954	238.2	0.289	1673.4
48_t_e1	48	Temperature	0.97	212.8	0.263	3908.3
168_t_e1	168	Temperature	0.974	215.3	0.375	3310.3
12_h_e1	12	Humidity	0.449	4032.5	-9.3	54520
48_h_e1	48	Humidity	0.522	3805.2	-9.1	53795
168_h_e1	168	Humidity	0.697	2546.8	-7.3	43798
12_ta_e1	12	Temperature-Ext. Aperture	0.995	38.2	0.786	1132.2
48_ta_e1	48	Temperature-Ext. Aperture	0.99	51.2	0.962	430.6
168_ta_e1	168	Temperature-Ext. Aperture	0.992	49.7	0.954	234.6
12_tha_e1	12	Temperature-Ext. Aperture-Humidity	0.991	50.0	0.979	60.3
48_tha_e1	48	Temperature-Ext. Aperture-Humidity	0.993	45.8	0.954	231.9
168_tha_e1	168	Temperature-Ext. Aperture-Humidity	0.989	57.8	0.835	827.4

12_ah_e1	12	Ext. Aperture-Humidity	0.994	48.5	0.961	199.9
48_ah_e1	48	Ext. Aperture-Humidity	0.994	48.7	0.951	256.6
168_ah_e1	168	Ext. Aperture-Humidity	0.993	47.9	0.961	200.1

Figure 35 below shows the model outputs when given a pass of the training dataset, compared to the ground truth of the extensometer aperture in the training dataset. The model output closely follows the seasonal trends, and in many instances, it follows intraday fluctuations and events, such as sudden spikes, adequately.

Figure 36 shows the model forecasts on the forecasting dataset, beginning on January 1st of 2023. The model is able to capture the overall trend, however the variance of the model increases from that of the ground truth trend, past January 20, 2023.

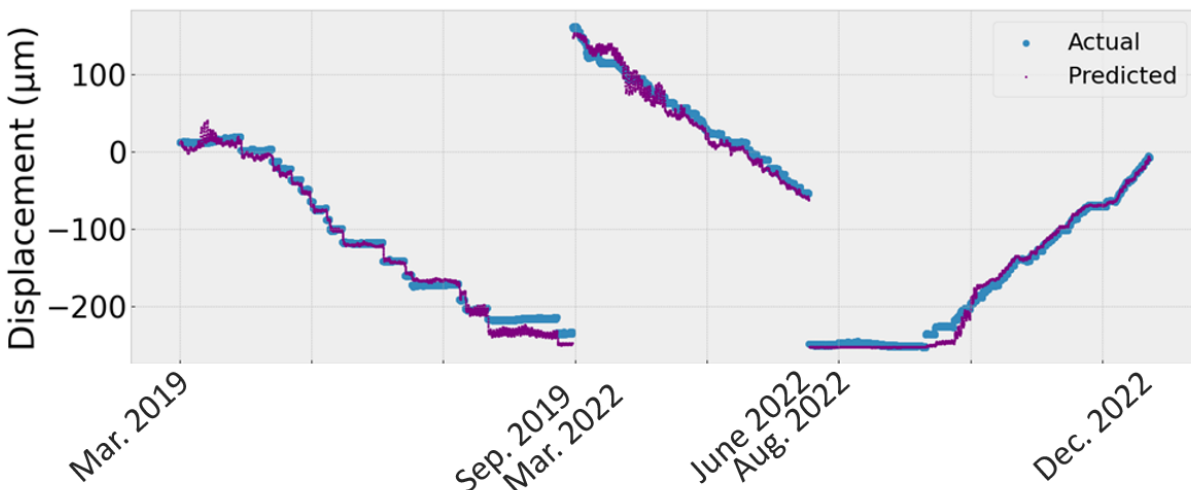

Figure 35: Test forecast on the training dataset for best performing model of extensometer 1.

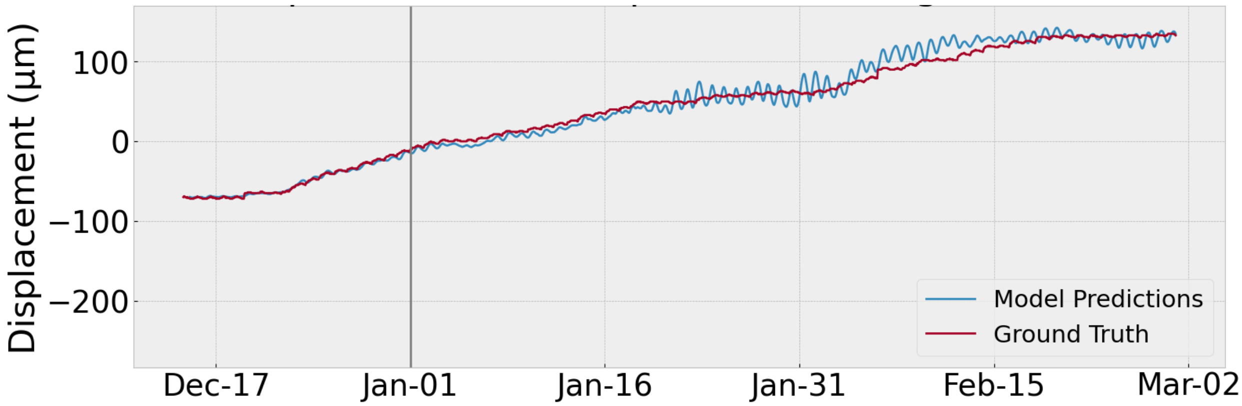

Figure 36: Extensometer 1 Forecast of best performing model on forecast dataset.

4.6.2 Modeling Extensometer 2

Most models for extensometer 2 performed well on the training and validation dataset, with R^2 scores exceeding 0.97 on all but the two shorter term lookback windows on the humidity models (Table 7). However, the model performance on the forecast dataset was very poor for all models, as reflected on the negative R^2 and high MSE values obtained for all models. The forecast of the extensometer 2 best performing model on the training dataset resemble the performance the extensometer 1 models had on it (Figure 37), by following the seasonal trends very well. In contrast, the extensometer 2 forecasted trend did not match the trend of the ground truth if the same period (Figure 38).

Table 7: Training, and Forecasting performance evaluations for Extensometer 2 CNN models

Model ID	Lookback Window (hrs)	input variables	Training R^2	Training MSE	Forecast R^2	Forecast MSE
12_t_e2	12	Temperature	0.975	59.2	-3.1	8779.7
48_t_e2	48	Temperature	0.990	51.0	-1.2	4873.5
168_t_e2	168	Temperature	0.990	51.1	-0.9	4183.9
12_h_e2	12	Humidity	0.721	1252.3	-13.3	30374.9
48_h_e2	48	Humidity	0.816	816.7	-8.8	21018.5
168_h_e2	168	Humidity	0.901	653.2	-10.8	25099.7
12_ta_e2	12	Temperature-Ext. Aperture	0.995	48.2	-0.2	2550.2
48_ta_e2	48	Temperature-Ext. Aperture	0.996	45.6	-0.2	2909.8
168_ta_e2	168	Temperature-Ext. Aperture	0.995	46.8	-0.2	2620.8

Model ID	Lookback Window (hrs)	input variables	Training R^2	Training MSE	Forecast R^2	Forecast MSE
12_tha_e2	12	Temperature-Ext. Aperture-Humidity	0.997	42.3	-0.4	3140.4
48_tha_e2	48	Temperature-Ext. Aperture-Humidity	0.995	43.5	-0.4	3207.4
168_tha_e2	168	Temperature-Ext. Aperture-Humidity	0.996	42.9	-0.2	2654.4
12_ah_e2	12	Ext. Aperture-Humidity	0.993	46.0	-1.0	4412.6
48_ah_e2	48	Ext. Aperture-Humidity	0.994	45.8	-0.9	3207.4
168_ah_e2	168	Ext. Aperture-Humidity	0.991	48.1	-1.0	2654.4

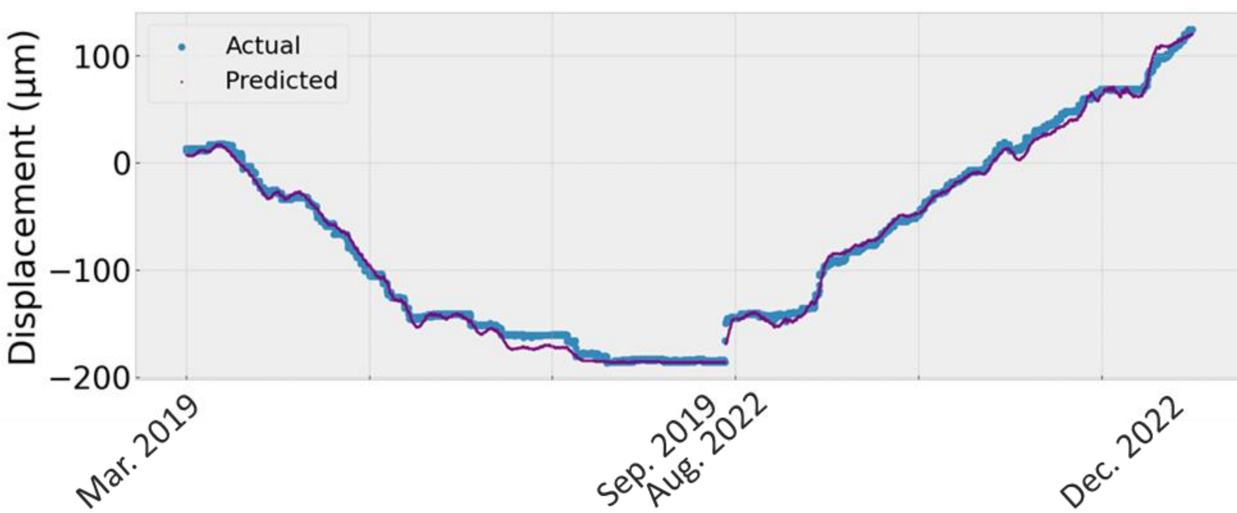

Figure 37:Test forecast on the training dataset for best performing model of extensometer 2

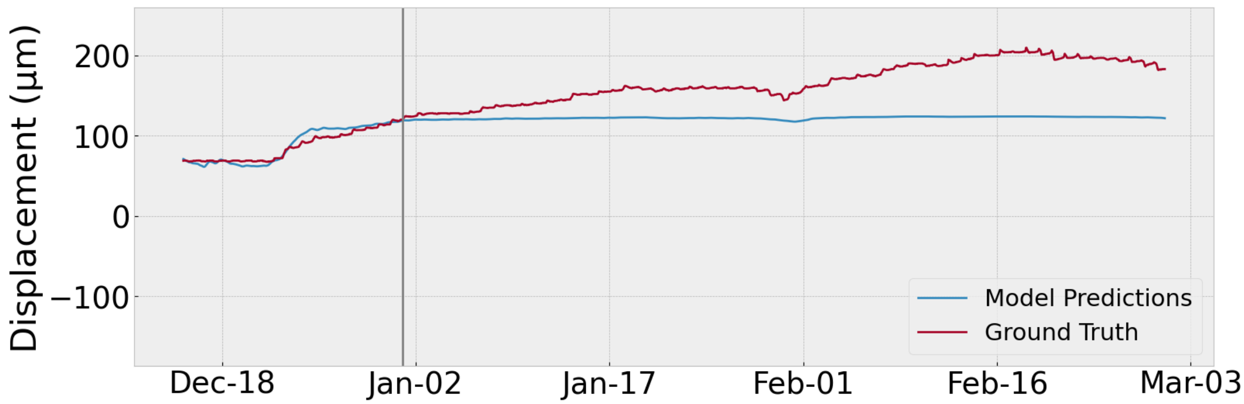

Figure 38: Extensometer 2 Forecast of best performing model on forecast dataset.

5 Discussion

5.1 Long Term Effect Of Thermally Induced Micromovements

In Figure 26 of subsection 4.3 a hysteretic pattern is observed on the temperature-displacement plot, with the extensometers' displacement in later monitoring years (from 2023 onwards) drifting away from their initial positions at the time of installation (15 Apr. 2019), moving towards a direction where both extensometers expand over time, (see Figure 39). After four years of monitoring, both extensometers have recorded a permanent displacement of approximately 100 μm away from their initial position.

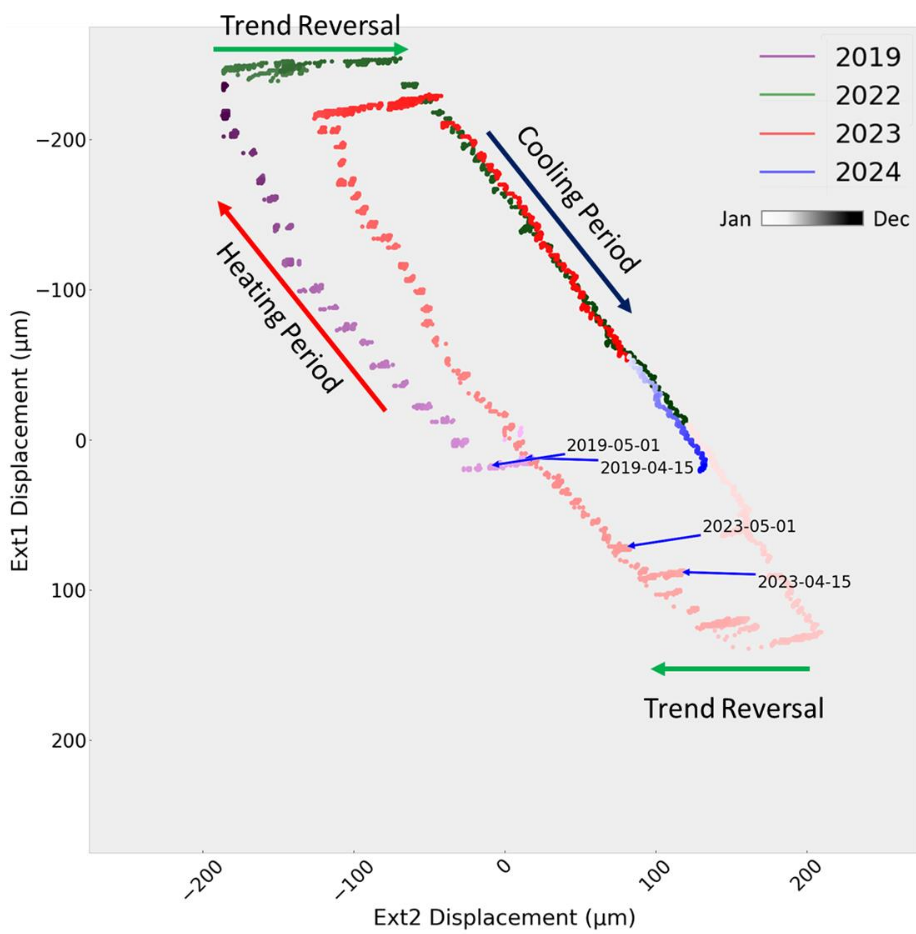

Figure 39: Difference in position of resultant vector after 4 years of monitoring. The pillar has not returned near its original position over time, hinting the existence of a "displacement drift" over time.

Figure 40: Fractured rock mass along on the ceiling of the South side of the main chamber

Figure 41: Exposed rock blocks suspended from the ceiling that look balanced by interlocking forces with neighboring blocks

The delicate structures within the rock mass, particularly evident at the exposed ceiling of the south chamber (Figure 40, Figure 41), comprise numerous individual rock blocks surrounded by infill and fractures extending from the ceiling void boundary to the main open fracture of the tomb. Many of these rock blocks appear to be standing solely due to interlocking with neighboring blocks, rendering them susceptible to disturbance. This arrangement results from the tilting of the SAQ hill block, where fractured, tilted blocks and their debris constitute the host rock mass of the tomb. During the excavation of the tomb, the exposed broken-up rock led to debris flows as material was excavated and removed, ultimately resulting in the catastrophic detachment of the wedge block from the tomb's ceiling.

While the temperature-induced movements initially may seem insignificant, continued aperture drift over an extended period could potentially lead to a configuration that allows an interlocked block to become loose and detached. Successive detached blocks may further exacerbate the situation by causing the release of even larger blocks due to the loss of support from previously interlocked blocks (Figure 42). If the detachment of the original wedge block was indeed the cause of the destruction of pillar H, it implies that the detachment of another block could result in damage to another pillar of the tomb. This could occur through the redistribution of overburden stress and an increase in the load supported by the pillar. Specifically, considering the isolated block supported by the critical pillar K, there exists a potential for overstressing and ultimate collapse of the pillar.

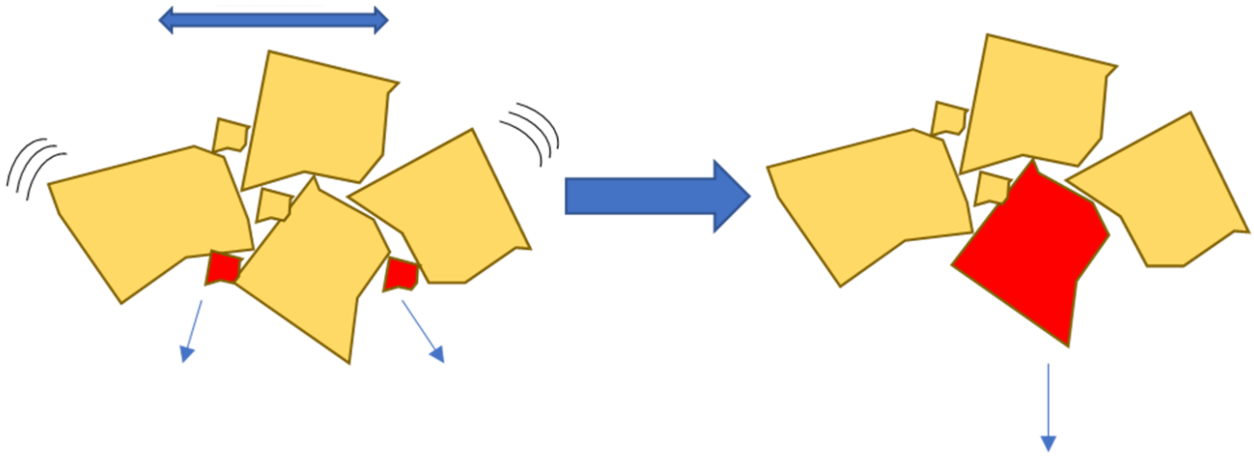

Figure 42: Micromovements measured by the extensometers could possibly disturbed the balanced interlocked individual rock blocks on the ceiling of TT95, leading to progressive detachment of neighboring interlocked blocks, and lead to stability issues.

To verify this hypothesis, a simple 2-Dimensional elastic model of the pillars of the south chamber was developed to identify pillars where might be overstressed [1]. Figure 43 shows the results of this analysis where an overstressed spot can be identified on the top of pillar K. If progressive disturbance of the rock mass due to continuous micromovements in the rock matrix continues for a long time, it is probable that rock material might be removed from the narrow cross-sectional area of the pillar top, which could lead to significant overstressing of the pillar.

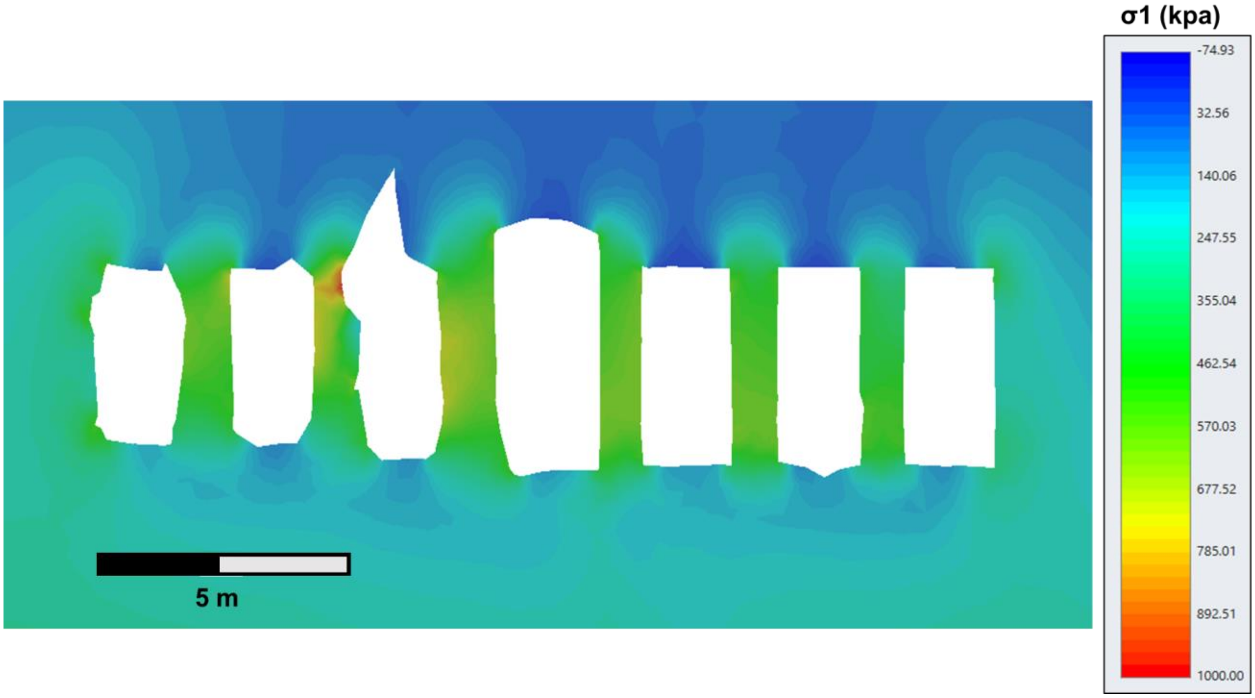

Figure 43: Preliminary elastic model results showing maximum principal stress contours for a North-South cross section of tomb TT95 through pillar K, with the highest stresses concentrated in the narrow section of pillar K.

5.2 Analysis On ML Results

Extensometer 1 results showed that the observed displacements can be forecasted by using the temperature, humidity and previous displacement history as inputs to the constructed CNN models. It also showed that omitting the extensometer history from the input set decreased the performance of the models.

This observation could be due to the fact that the pure climatic time series alone are not sufficient to forecast the pillar displacements, due to the absence of an input variable that describes the rock behaviour. The displacements that are being measured depend largely on the rock material (the displacements are the observed response of the rock material to some input, and thus depend on it) and the geometrical configuration of the tomb and the monitoring setup (placement of extensometers, foliation plane direction relative to instrument orientation).

The displacement history when passed as an input to the model embeds this information on the response curve of the time series. It serves as a proxy to material characteristics of the rock that are unknown, but do not need to be quantified, thus eliminating bias when trying to quantify material parameters for modelling the rock material itself.

The downside of this is that the model has only seen the conditions of the exact configuration it was trained on. If the extensometers were moved and reinstalled at a different pillar, the models need to be updated by collecting data on the newly placed system and retrain the models using the new measurements. This is impractical as data collection requires a significant time investment and effort to create new models, retrain them, revalidate them and use them to make forecasts.

The poor performance on the models trained with extensometer 2, could be partially owed to the fact that extensometer 2 had less data available for training than extensometer 1, due to the instrument malfunction during the heating period of 2022. This lack of observations could be the potential cause of the severe overfitting issue observed with the extensometer 2 models. As the monitoring system is collecting more data, the data availability issue can be eventually mitigated, by continuously retraining the Extensometer 2 ML models weekly, as more data become available until performance improves.

If extensometer 2 forecasts improve as a result of the above, the machine learning models for the two extensometers could be used to make projections for the future state of the extensometer displacements by using the real-time climatic data as inputs to the model. This can provide the opportunity of making future forecasts about the displacements which can be utilized to develop what-if scenarios using future climatic projections as input to the established models, for assessing the future stability state of the tomb. The range of forecasted future displacements in this scenario can then provide useful information about the future stability of the tomb, as displacement patterns can shed light about the structural stability of the pillar. The forecasted displacements can also be used to calibrate numerical models for stress analysis of the pillar and the tomb in its entirety to structurally assess the future state of the tomb, enabling for proactive action by informing on how the tomb should be rehabilitated. In doing so it should be noted that the forecasting timeframe for which the forecast results can be trusted need to be determined by performing an uncertainty analysis for the developed models, which falls outside of the scope of the research presented here.

To conclude, the ML methodology used in this research yielded inconclusive results and did not meet the objective of the research. On one hand, the models created from this methodology were able to provide accurate forecasts for extensometer 1, while failed to meet a similar forecasting ability for extensometer 2. Continuing the data collection further and developing a more rigorous methodology in which hyperparameter tuning of the selected CNN architectures is carefully done, might fix the overfitting issue with extensometer 2.

5.3 Challenges Related To Data Collection

Data collection challenges are important to list and discuss as they provide valuable insights on the interpretation stage and can be a valuable reference for future monitoring projects. The case of TT95 is a great example of describing what can go wrong during the data collection process as numerous problems arose in the data collection stage. A significant outtake of examining these issues is to provide a basis for careful planning and considerations that need to be taken for similar monitoring setups and environments.

5.3.1 Power Source

A big part of installing a monitoring system is securing a reliable power source to power up the instruments and logging devices. This is particularly important for projects happening in remote locations where power supplied from the nearest grid is impossible. In the absence of The SAQ hill is located at a close proximity to Luxor, and, perhaps due to the touristic interest it generates, the tombs are illuminated at night by a group of projectors. The power requirement for the lighting equipment meant that grid power was available in the hill, and thus it became a usable power source for the monitoring equipment in TT95.

Despite the availability of power, the reliability of the grid should not be taken for granted. The uptime of the grid can be questionable, and considerations about power interruptions should be taken on the planning stage of any monitoring project, as they can lead to gaps in data collected. To target this, our system also included a battery as a back-up power source in periods where grid power was interrupted. When grid-based power was available, the system was powered from the grid and the battery was being charged. On the other hand, when power was interrupted, the battery was able to supply the system with the power it needed.

5.3.2 Environmental factors

Another factor threatening the efficiency and uptime of the monitoring system can be attributed to the environmental conditions of the system. TT95 remains sealed for large periods of time. Because of this, there is a lack of ventilation and air circulation inside the tomb, which, combined with the high average temperatures that can be reached, provides the risk of having parts of the equipment, such as the Raspberry Pi logger, overheat which can disturb their operation. To mitigate this, the Raspberry Pi was placed inside a plastic case, with little fans placed inside the box to provide some airflow and reduce the risk of overheating.

6 CONCLUSION

The research described in the preceding chapters focused on addressing 4 main objectives. Specifically, this research aimed to collect data on long-term behaviour on shallow excavations, by studying the structure and host rock of TT95, an ancient Egyptian tomb that has been exposed to climatic variations for thousands of years. Second, this study also aimed to add on to the existing knowledge base on environmentally driven rock degradation mechanisms as those have been observed on laboratory experiments or in-situ exposed rock surface monitoring. In addition, it targeted on developing a data-driven methodology for analyzing the collected data and gain insights of how environmental variations affect the rock mass behaviour of the TT95 host rock.

All the above areas are combined with the last objective this research aimed to address, which is establishing a knowledge basis which can be used as input to develop guidelines for future potential rehabilitation of TT95 and other similar structures in the tomb cluster of the SAQ hill. The above objectives have been addressed by the following points:

- A monitoring equipment was installed in TT95 for collecting in-situ climatic measurements of temperature and relative humidity inside and outside the tomb. Two extensometer displacements were also installed, measuring the relative displacement between a damaged pillar and its neighbouring pillar, and the damaged pillar with the excavation wall. The system started collecting data in April of 2019, collecting over 4 years of data, but technical difficulties related to the equipment caused gaps in measurements.

- Exterior ambient air temperatures ranged from 14.4^0C to 47.0^0C, while interior temperatures in the tomb ranging between 23.5 to 33.5^oC. Relative humidity ranged from 1 to 47% in ambient air outside TT95, with humidity inside the chapel ranging from 8 to 21%. The extensometer displacements ranged within an amplitude of 0.4 mm.
- Extensometer displacements exhibit high inverse correlation with the temperature fluctuations on the interior of the tomb with a Pearson-R correlation value in the interval (-0.93,-0.91). Displacement-temperature plots revealed the potential presence of a hysteretic effect, similar to what has been observed in the literature in projects monitoring fracture aperture in exposed rock surfaces, with a yearly displacement drift of approximately 0.02 mm/year.
- ML models based on a CNN architecture were created and trained on the collected sensor data. The inputs to the models consisted of different combinations of sensor data time-series, along with a varying amount of data points that the models would use for making forecasts. The models for extensometer 1 performed excellent on the forecasts, with an R^2 score of 0.98 on the best performing model, but extensometer 2 performed poorly with a best R^2 of -0.2. The best performing model for extensometer 1 used temperature, humidity and past displacement history as inputs to the model, with a lookback time of window of 12 hours. The best performing model for extensometer 2 used temperature and extensometer displacement history as inputs to the model and a lookback time of 48 hours.
- The yearly drift of extensometer displacements could disturb loose material from the ceiling of TT95 by the continuous opening and closing cycles and permanent displacement of fractures within the rock mass as they react to temperature fluctuations. Due to the rock quality and the disintegrated rock mass with loose interlocked rock blocks in the ceiling of TT95, continuous disturbance could

potentially cause the release of one or more loose rock pieces from the ceiling of TT95 overtime.

To summarize, a monitoring system was installed on the interior of the ancient Egyptian funerary chapel TT95, located along the side of the SAQ hill, in the UNESCO Designated World Heritage site of the Theban Necropolis, near Luxor, Egypt. The monitoring system collected data of temperature and humidity fluctuations, along with relative displacements from two extensometers installed between a damaged pillar with its adjacent one, and the chapel's wall. Exploratory data analysis performed on the collected dataset revealed a cyclic behaviour of the extensometer displacements over time, with high inverse correlation with the interior temperature of the tomb. The analysis also revealed a hysteresis pattern, with a yearly extensometer drift. A machine learning methodology was developed to forecast future extensometer displacements by utilizing the collected monitoring data as inputs to CNN based models. Lastly, a potential long-term failure mechanism for the tomb owed to disturbance of the rock fabric over time due to perturbations and micromovements within the rock mass as it responds to humidity and temperature trends was proposed for TT95.

The results of this study gave an insight into how environmental changes can affect the host rock of TT95. The monitoring data collected in this study provide a basis for future research. The data collected can be used to calibrate thermomechanical numerical models that can answer more questions on the outlook of the stability of TT95 in the future as it continues being exposed to environmental fluctuations. Additionally, the machine learning methodology and forecasting performance can be improved as more data become available, which also provides an opportunity for comparing the data-driven modelling approach with results obtained from numerical analysis.

BIBLIOGRAPHY

[1] A. , A.-O. R. L.-G. A. , B. S. , Z. M. , K. U. T. , P. M. A. Vasileiou, “Numerical and machine learning based approaches to study the influence of environmental conditions on crack growth in the Theban Necropolis, Egypt,” in *22nd Canadian Rock Mechanics Symposium*, Kingston, Ontario: Canadian Rock Mechanics Assossiation, 2022.

[2] M.-P. Aubry *et al.*, “Pharaonic necrostratigraphy: a review of geological andarchaeological studies in the Theban Necropolis, Luxor, WestBank, Egypt”, doi: 10.1111/j.1365-3121.2009.00872.x.

[3] “About the TMP | Theban Mapping Project.” Accessed: Sep. 21, 2021. [Online]. Available: https://thebanmappingproject.com/about

[4] A. Loprieno-Gnirs, *Life histories of Theban tombs : transdiciplinary investigations of a cluster of rock-cut tombs at Sheikh ’Abd el-Qurna*. Cairo: The American University in Cairo Press, 2021.

[5] R. Alcaíno-Olivares, M. Ziegler, S. Bickel, H. Ismaiel, K. Leith, and M. Perras, “Rock Mechanical Laboratory Testing of Thebes Limestone Formation (Member I), Valley of the Kings, Luxor, Egypt,” *Geotechnics*, vol. 2, no. 4, 2022, doi: 10.3390/geotechnics2040040.

[6] P. K. Gautam *et al.*, “Damage Characteristics of Jalore Granitic Rocks After Thermal Cycling Effect for Nuclear Waste Repository,” vol. 54, pp. 235–254, 2021, doi: 10.1007/s00603-020-02260-7.

[7] G. Feng, X. Wang, Y. Kang, and Z. Zhang, “Effect of thermal cycling-dependent cracks on physical and mechanical properties of granite for enhanced geothermal system,” *International Journal of Rock Mechanics & Mining Sciences*, vol. 134, p. 104476, 2020, doi: 10.1016/j.ijrmms.2020.104476.

[8] Y. Gunzburger, V. Merrien-Soukatchoff, and Y. Guglielmi, “Influence of daily surface temperature fluctuations on rock slope stability: case study of the Rochers

de Valabres slope (France)," *International Journal of Rock Mechanics & Mining Sciences*, vol. 42, pp. 331–349, 2005, doi: 10.1016/j.ijrmms.2004.11.003.

[9] M. Gasc-Barbier, V. Merrien-Soukatchoff, D. Virely, M. Gasc-Barbier, V. Merrien-Soukatchoff, and D. Virely, "The role of natural thermal cycles on a limestone cliff mechanical behaviour," *Eng Geol*, vol. 293, p. 106293, 2021, doi: 10.1016/j.enggeo.2021.106293ï.

[10] B. D. Collins and G. M. Stock, "Rockfall triggering by cyclic thermal stressing of exfoliation fractures," *Nat Geosci*, vol. 9, no. 5, pp. 395–400, May 2016, doi: 10.1038/ngeo2686.

[11] B. D. Collins and G. M. Stock, "Rockfall triggering by cyclic thermal stressing of exfoliation fractures," 2016, doi: 10.1038/NGEO2686.

[12] S. Hemeda, "Geo-environmental monitoring and 3D finite elements stability analysis for site investigation of underground monuments. Horemheb tomb (KV57), Luxor, Egypt," vol. 9, p. 17, 2021, doi: 10.1186/s40494-021-00487-3.

[13] S. Hemeda, "Engineering failure analysis and design of support system for ancient Egyptian monuments in Valley of the Kings, Luxor, Egypt," *Geoenvironmental Disasters*, vol. 5, no. 1, Dec. 2018, doi: 10.1186/s40677-018-0100-x.

[14] R. A. J. Wüst and J. McLane, "Rock derioration in the royal tomb of seti I, valley of the kings, Luxor, Egypt," 2000. doi: 10.1016/S0013-7952(00)00057-0.

[15] S. Hemeda, "Engineering failure analysis and design of support system for ancient Egyptian monuments in Valley of the Kings, Luxor, Egypt," *Geoenvironmental Disasters*, vol. 5, no. 1, Dec. 2018, doi: 10.1186/s40677-018-0100-x.

[16] American Research Center in Egypt, "Theban Mapping Project."

[17] "Google Earth Pro 7.3, Luxor, 25 42' 15" - 32 37' 58" Elevation 13.86km," 2023.

[18] C. Dupuis *et al.*, "Genesis and geometry of tilted blocks in the Theban Hills, near Luxor (Upper Egypt)," *Journal of African Earth Sciences*, vol. 61, no. 3, pp. 245–267, Oct. 2011, doi: 10.1016/J.JAFREARSCI.2011.06.001.

[19] M. Ziegler, R. Collderweih, A. Wolter, and A. Loprieno-Gnirs, “Rock mass quality and preliminary analysis of the stability of ancient rock-cut Theban tombs at Sheikh ‘Abd el-Qurna, Egypt”, doi: 10.1007/s10064-019-01507-0.

[20] R. Wüst, “Geologisch-geotechnische Untersuchungen im thebanischen Gebirge, Teil Süd, Luxor, Ägypten.,” University Bern, 1995.

[21] G. Curtis, “The geology of the Valley ofthe Kings, Thebes, Egypt.,” 1979.

[22] I. H. Sarker, “Machine Learning: Algorithms, Real-World Applications and Research Directions,” 2021. doi: 10.1007/s42979-021-00592-x.

[23] A. Grosan Crina and Abraham, “Artificial Neural Networks,” in *Intelligent Systems: A Modern Approach*, Berlin, Heidelberg: Springer Berlin Heidelberg, 2011, pp. 281–323. doi: 10.1007/978-3-642-21004-4_12.

[24] P. Munro, “Backpropagation,” in *Encyclopedia of Machine Learning*, C. Sammut and G. I. Webb, Eds., Boston, MA: Springer US, 2010, p. 73. doi: 10.1007/978-0-387-30164-8_51.

[25] L. Alzubaidi *et al.*, “Review of deep learning: concepts, CNN architectures, challenges, applications, future directions,” *J Big Data*, vol. 8, no. 1, 2021, doi: 10.1186/s40537-021-00444-8.

[26] S. Teng, G. Chen, Z. Yan, L. Cheng, and D. Bassir, “Vibration-based structural damage detection using 1-D convolutional neural network and transfer learning,” *Struct Health Monit*, vol. 22, no. 4, 2023, doi: 10.1177/14759217221137931.

[27] O. Abdeljaber, O. Avci, S. Kiranyaz, M. Gabbouj, and D. J. Inman, “Real-time vibration-based structural damage detection using one-dimensional convolutional neural networks,” *J Sound Vib*, vol. 388, 2017, doi: 10.1016/j.jsv.2016.10.043.

[28] J. Kim, S. Oh, H. Kim, and W. Choi, “Tutorial on time series prediction using 1D-CNN and BiLSTM: A case example of peak electricity demand and system marginal price prediction,” *Eng Appl Artif Intell*, vol. 126, 2023, doi: 10.1016/j.engappai.2023.106817.

[29] W. W. Gay, *Raspberry Pi Hardware Reference*. 2014. doi: 10.1007/978-1-4842-0799-4.

[30] Digi Inc, “Arduino UNO Reference Design,” Arduino.

[31] R. Guido van and P. development Team, “The Python Language Reference,” *Python Software Foundation*, 2013.

[32] F. Pedregosa *et al.*, “Scikit-learn: Machine learning in Python,” *Journal of Machine Learning Research*, vol. 12, 2011.

[33] J. D. Hunter, “Matplotlib: A 2D graphics environment,” *Comput Sci Eng*, vol. 9, no. 3, 2007, doi: 10.1109/MCSE.2007.55.

[34] C. Hill, “SciPy,” in *Learning Scientific Programming with Python*, 2016. doi: 10.1017/cbo9781139871754.008.

[35] S. Van Der Walt, S. C. Colbert, and G. Varoquaux, “The NumPy array: A structure for efficient numerical computation,” *Comput Sci Eng*, vol. 13, no. 2, 2011, doi: 10.1109/MCSE.2011.37.

[36] W. McKinney and P. D. Team, “Pandas-Powerful python data analysis toolkit,” *Pandas—Powerful Python Data Analysis Toolkit*, vol. 1625, 2015.

[37] H. R. Maier and G. C. Dandy, “Neural networks for the prediction and forecasting of water resources variables: A review of modelling issues and applications,” *Environmental Modelling and Software*, vol. 15, no. 1, 2000, doi: 10.1016/S1364-8152(99)00007-9.

Numerical and machine learning based approaches to study the influence of environmental conditions on crack growth in the Theban Necropolis, Egypt

Vasileiou, A.[1], Alcaino-Olivares, R.[1], Loprieno-Gnirs, A.[2], Bickel, S.[2], Ziegler, M.[3], Khan, U.T.[1], Perras, M.A.[1]
[1]Department of Civil Engineering, York University, Toronto, Ontario, Canada.
[2]Department of Ancient Civilizations – University of Basel, Basel, Switzerland
[3]Department of Earth Sciences, Swiss Federal Institute of Technology – ETH, Zurich, Switzerland

Background

The Thebes Necropolis in Luxor, Egypt, was listed by UNESCO as a World Heritage site in 1979. During the Egyptian New Kingdom (1500 – 1000 BC) many rock-cut tombs were constructed to host funerary chambers for the high cast society, of which 450 of them have been uncovered to-date [1]. The area extends over 6 km² and includes marl and limestone from the Thebes Limestone Formation (Lower Eocene), with structural features such as listric faults, networks of gullies and steep cliffs all across the Thebes Mountains. Efforts have been made to better understand the geo-hazards which could jeopardize the preservation of Theban Necropolis. The tombs in Theban Necropolis have been exposed environmental fluctuations for thousands of years. Previous monitoring work, near tomb KV 42 in the Valley of the Kings, showed that current fluctuations in ambient temperature and humidity correlate with movement of a large vertical crack (Fig. 1a), separating a rock column from the main bedrock of the cliffs (Fig. 1b) [2].

The specific objectives of this research are

- Understand the past and potential future long term failure mechanisms
- Influence of the contribution of environmental parameters on crack growth
- Investigate opportunities to forecast future crack growth based on Machine Learning algorithms
- Applying the research findings to long term preservation of the tombs in Theban Necropolis

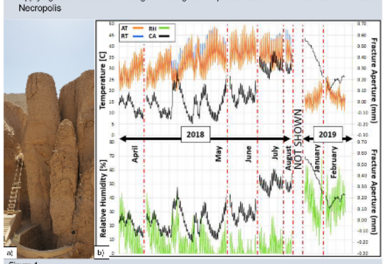

Figure 1

TT95 is a rock-cut tomb located on the hill Sheikh Abd el-Qurna (SAQ), about 1km south-east of KV42 (Fig. 2a). A large through going open fracture crosses the eastern chamber of the tomb and was a release plane for a large wedge that collapsed during the construction of the tomb, according to archaeological evidence. A critical pillar (pillar K) is located on the fracture plane, which cuts through it (Fig. 2d).

Monitoring Installation

The team installed a monitoring station inside TT95 consisting of:

- 2 Yield Point extensometers (E1 & E2) measuring the relative displacement between pillar K and pillar J, and pillar K with the western wall of the first chamber (Fig. 2b)
- 2 thermal sensors integrated into the extensometers
- 2 climate sensors measuring the ambient temperature and relative humidity inside and outside of the tomb
- RockMass's Axis Mapper (Fig. 2c) for fracture scanning
- An array of 10 thermal sensors (R# in bottom right illustration) that are installed at several elevations along pillar K and the fracture on the roof (Fig. 2e)

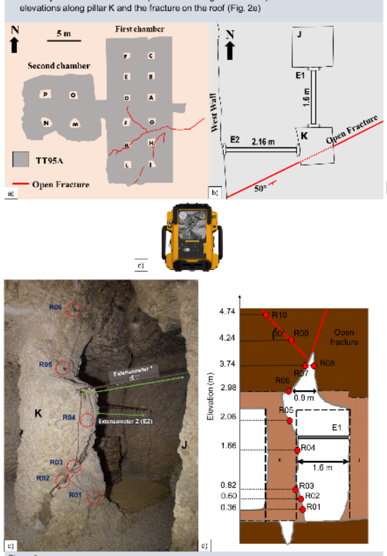

Figure 2

Monitoring Results

- Continuous, hourly, monitoring was conducted from April 15, 2019 to August 16, 2019, until power was unexpectedly cut off
- During this period, temperatures rose quickly until mid-June, after which daily fluctuations remain constant and there is no long term change in temperature (Fig. 3a)
- The temperature in the interior of the tomb is much more stable and rises slowly over time
- Relative humidity remains higher inside TT95 and follows a slightly increasing trend; high humidity fluctuations are observed on the exterior of the tomb (Fig. 3b)

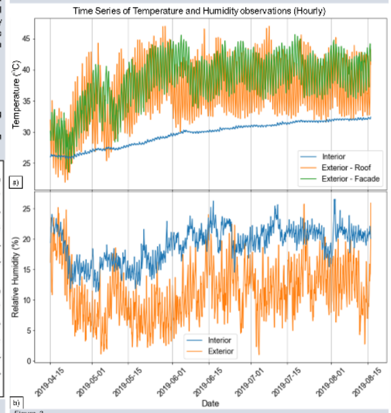

Figure 3

- Measured displacements show that pillar K converges towards the West Wall and pillar J (Fig. 4a)
- The displacements seem to correlate with the increase in temperature, converging faster during the intense heating of the first few weeks, and slowing down when temperature fluctuations stabilize
- The measurements show distinct jumps in displacement at regular intervals as the extensometers shorten; This could be an indication of crack propagating and releasing strain energy, or may indicate slippage of the instruments along the pillars, triggered by their movement
- The top of the pillar is heating faster than its bottom, creating a temperature gradient along the pillar (Fig. 4b)
- These findings agree with what was observed near KV42, suggesting that temperature and humidity fluctuations may play a role in the fracture aperture fluctuations

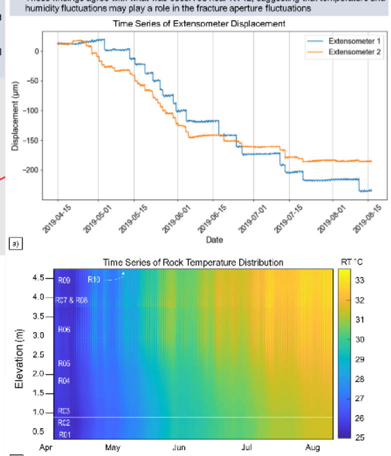

Figure 4

Acknowledgements

This project is supported in part by funding from the Government of Canada's New Frontiers in Research Fund (NFRF) (Grant Number: [NFRF-2020-00893])

Ce projet est financé en partie par le fonds Nouvelles frontières en recherche du gouvernement du Canada

The team would also like to acknowledge:

- YieldPoint Inc. and Andrew Hyett for sponsoring the instrumentation equipment
- Rockmass for allowing us to use the axis mapper, as well as Shelby Yee and Jessica Andrew for their interest and support to the project

Numerical Modelling

A 3-dimensional mechanical Finite Element Model of TT95 is being developed using Rocscience's, RS3. Point clouds from photogrammetric scans of the interior and exterior of the tomb were utilised to create the 3D geometry of the model [3]. The geometry was simplified to reduce computational time (Fig. 5a & 5b). A simple elastic model was developed initially to identify stress concentrations around the excavation and give insight to areas of concern (Fig. 5c). At present the open fracture has not been modelled, however, it will significantly impact the stresses and displacements near pillar K and is planned for future work.

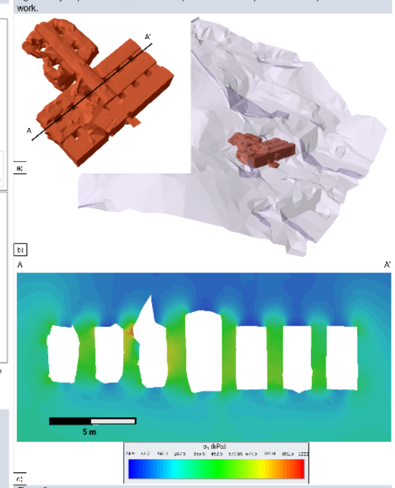

Figure 5

Use of Machine Learning to Forecast Displacement

Artificial Neural Networks (ANNs) are supervised Machine Learning algorithms that can be used to exploit relationships between variables and create predictive models. In this work, an ANN was used to predict the displacement of the extensometers using lagged exterior temperature and previous displacements, up to four days before each observation (t-1,…,t-4) (Fig. 6a). The model showed promising performance on the training dataset, but overestimated displacements on the testing dataset (Fig. 6b). This is an indication that the algorithm overfits the training dataset, and hyperparameter tuning of the model is needed. Additionally, training the model on more inputs (humidity, rock temperature distribution, etc.) could also contribute to increase the training performance.

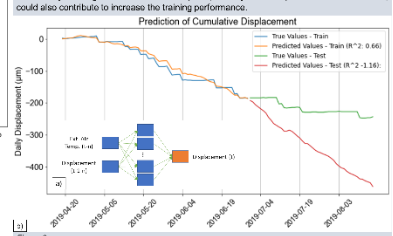

Figure 6

Future Work

- Visit the site to maintain the monitoring equipment, and receive new data for 2022
- Use the axis mapper to rescan the fractures of the tomb
- Update the mechanical model to use a Hoek-Brown material behaviour and introduce the open fracture discretely
- Consult with the archaeological team to implement the construction sequence in the model staging to capture the roof collapse
- Continue the development of ANN to increase forecasting accuracy
- Make recommendations for long term preservation of the tomb

References

[1] Loprieno-Gnirs A. 2018. Creuser une tombe dans la colline thébaine: le project archéologique ***Life Histories of Theban Tombs*** de l'université de Bâle. Bulletin de la Société française d'égyptologie 199, pp. 100-126.
[2] Alcaino-Olivares R., Perras M.A., Ziegler M., Leith K. 2020. Thermo-Mechanical Cliff Stability at Tomb KV42 in the Valley of the Kings, Egypt. In: Sassa K., Mikoš M., Sassa S., Bobrowsky P.T., Takara K., Dang K. (eds) Understanding and Reducing Landslide Disaster Risk. WLF 2020.
[3] Ziegler, M., Collдeweih, R., Wolter, A. and Loprieno-Gnirs, A. 2019. Rock mass quality and preliminary analysis of the stability of ancient rock-cut Theban tombs at Sheikh 'Abd el-Qurna, Egypt. Bulletin of Engineering Geology and the Environment 78(8), pp.6179-6205.
[4] Wilkinson, RH & Weeks, KR. 2014. The Oxford Handbook of the Valley of the Kings. New York: Oxford University Press.